iScience

CellPress
OPEN ACCESS

Article

Cortical brain organoid slices (cBOS) for the study of human neural cells in minimal networks

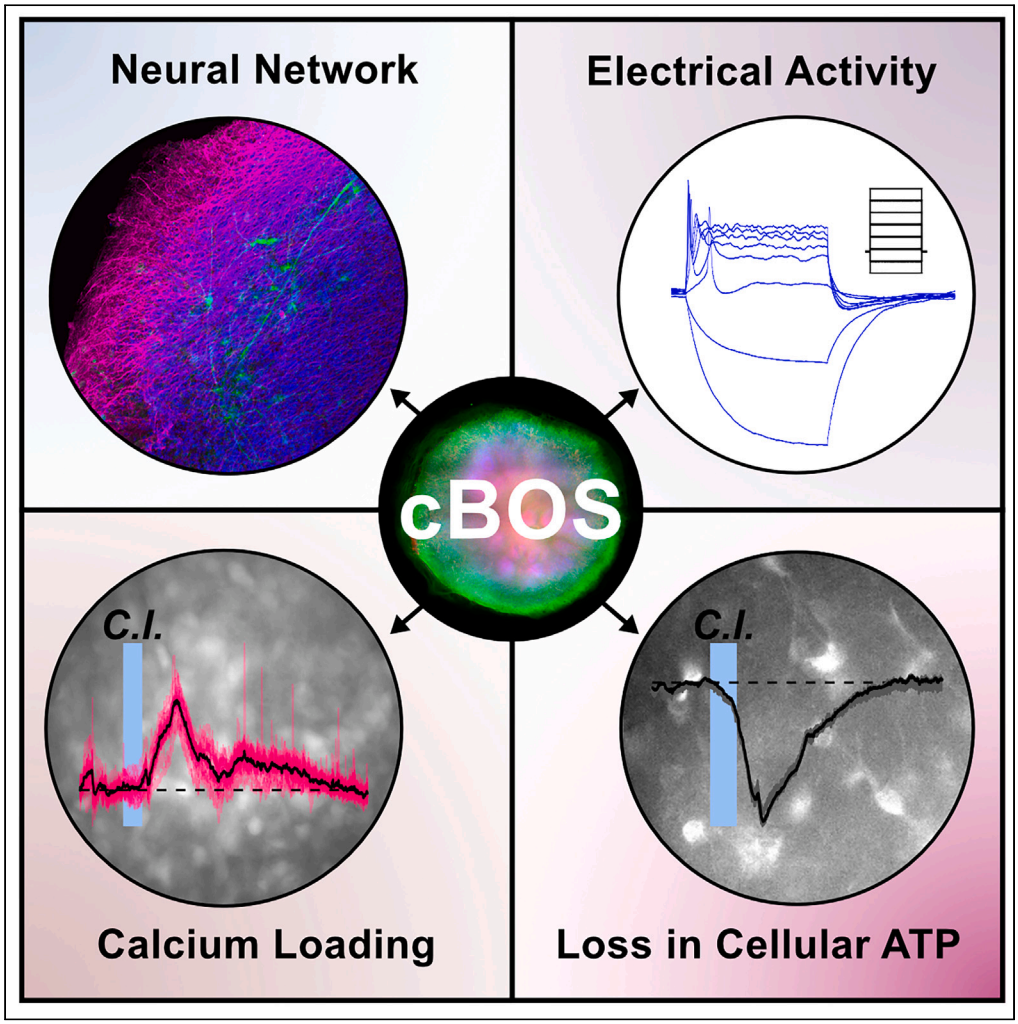

Laura Petersilie, Sonja Heiduschka, Joel S.E. Nelson, ..., Karl W. Kafitz, Alessandro Prigione, Christine R. Rose

Alessandro.Prigione@med.uni-duesseldorf.de (A.P.)
rose@hhu.de (C.R.R.)

Highlights

cBOS are organized cell models hosting mature neural networks and astrocytes

cBOS allow functional analysis of cortical human neural cells and networks

cBOS undergo intracellular Ca^{2+} loading with brief application of chemical ischemia

Chemical ischemia in cBOS causes an immediate decrease in cellular ATP

Petersilie et al., iScience 27, 109415
April 19, 2024
https://doi.org/10.1016/j.isci.2024.109415

iScience

CellPress
OPEN ACCESS

Article

Cortical brain organoid slices (cBOS) for the study of human neural cells in minimal networks

Laura Petersilie,[1] Sonja Heiduschka,[2] Joel S.E. Nelson,[1] Louis A. Neu,[1] Stephanie Le,[2] Ruchika Anand,[3] Karl W. Kafitz,[1] Alessandro Prigione,[2,4,*] and Christine R. Rose[1,4,5,*]

SUMMARY

Brain organoids derived from human pluripotent stem cells are a promising tool for studying human neurodevelopment and related disorders. Here, we generated long-term cultures of cortical brain organoid slices (cBOS) grown at the air-liquid interphase from regionalized cortical organoids. We show that cBOS host mature neurons and astrocytes organized in complex architecture. Whole-cell patch-clamp demonstrated subthreshold synaptic inputs and action potential firing of neurons. Spontaneous intracellular calcium signals turned into synchronous large-scale oscillations upon combined disinhibition of NMDA receptors and blocking of $GABA_A$ receptors. Brief metabolic inhibition to mimic transient energy restriction in the ischemic brain induced reversible intracellular calcium loading of cBOS. Moreover, metabolic inhibition induced a reversible decline in neuronal ATP as revealed by ATeam1.03^{YEMK}. Overall, cBOS provide a powerful platform to assess morphological and functional aspects of human neural cells in intact minimal networks and to address the pathways that drive cellular damage during brain ischemia.

INTRODUCTION

Studying the human brain and its development is crucial if we want to understand how neurological and neurodevelopmental disorders arise. However, although these diseases are a leading cause of disability worldwide,[1,2] the complexity of the human brain hampers the establishment of approaches aiming at unveiling mechanistic disease aspects. Investigating neuronal disorders in patients is challenging due to the inaccessibility of brain cells. Moreover, peripheral cells and postmortem investigations provide only limited help for capturing disease-initiating events.[3] Animal models also exhibit important limitations, given the unique aspects of human neurodevelopment that are not recapitulated in rodents.[4] These differences can be appreciated also macroscopically, as the human brain is gyrencephalic, while the rodent brain is lissencephalic.[5,6] Indeed, some human neurological and neurodevelopmental diseases cannot be easily reproduced in rodents, hindering the translation of animal research to human medical applications.

A major breakthrough in studying human brain development came from the discovery that human pluripotent stem cells (hPSCs) can be coaxed into three-dimensional (3D) structures that recapitulate features of the developing human brain.[7,8] These structures, defined as neural organoids or brain organoids, are now being recognized as an important tool to gain essential information with respect to human neurodevelopment and its related disorders.[3,9,10] In fact, brain organoids can reproduce key features of the fetal human brain, including its cellular architecture, cell composition and diversity, and neural maturation.[9,11] Brain organoids can also exhibit network-like activity suggesting the presence of neural communication.[12] For these reasons, in recent years there has been an increasing amount of studies demonstrating how brain organoids can be used to model neurological and neuropsychiatric diseases to capture pathological mechanisms and unveil targets of intervention.[7,13–15]

Despite these important advances, key aspects related to 3D brain organoids still require improvement. In fact, it has become clear that upon continued growth of brain organoids in 3D, cellular maturation and viability are hampered by an insufficient delivery of oxygen and nutrients to their core regions.[16,17] Because of this, brain organoids in 3D do not increase beyond a certain size, as they gradually develop cell death in the central regions. In addition, the structure of large-diameter 3D brain organoids complicates the direct probing of neuronal functionality. To circumvent these limitations, several laboratories have recently introduced long-term culturing of slices prepared from whole-brain cerebral organoids grown at the air-liquid interphase (ALI-COs).[18,19] Such cultures of sliced organoids show reduced cell death in the central region and improved growth and cellular maturation as compared to 3D brain organoids.[18,20–22] Moreover, cultured brain

[1]Institute of Neurobiology, Faculty of Mathematics and Natural Sciences, Heinrich Heine University Duesseldorf, 40225 Duesseldorf, Germany
[2]Department of General Pediatrics, Neonatology and Pediatric Cardiology, University Children's Hospital and Heinrich Heine University Duesseldorf, 40225 Duesseldorf, Germany
[3]Institute of Biochemistry and Molecular Biology I, Medical Faculty and University Hospital Duesseldorf, Heinrich Heine University Duesseldorf, 40225 Duesseldorf, Germany
[4]Senior author
[5]Lead contact
*Correspondence: Alessandro.Prigione@med.uni-duesseldorf.de (A.P.), rose@hhu.de (C.R.R.)
https://doi.org/10.1016/j.isci.2024.109415

organoid slices enable a more direct access to the tissue, facilitating the implementation of functional assessment of the developing neural network e.g., through multielectrode array (MEA) recordings or cellular calcium imaging.[18,21–24]

In the present work, we followed this strategy and report a protocol for establishing robust cortical brain organoid slices (cBOS) derived from regionalized cortical organoids that can be maintained in prolonged culture at the air-liquid interface. Given the homogeneous and spherical morphology of cortical organoids, cBOS show a uniform roundish appearance and develop well-organized and connected structures of neurons and astrocytes. Single-cell electrophysiological recordings revealed subthreshold synaptic inputs and neuronal action potential firing whereas calcium imaging demonstrated spontaneous intracellular calcium transients as well as large synchronous oscillations upon disinhibition, indicating that cBOS represent a functionally active, synaptically connected neural network. Exposure of cBOS to pharmacological inhibitors of glycolysis and oxidative phosphorylation to mimic hypoxic-ischemic conditions resulted in a rapid increase in intracellular calcium concentrations. The increase in cellular calcium was accompanied by an immediate loss of cellular ATP. In conclusion, these results demonstrate that ATP depletion under ischemic conditions induces cellular calcium loading in a developing human cortical network in culture. Furthermore, they suggest that cBOS may serve to elucidate the molecular pathways and consequences of ischemia-induced rapid ion dysregulation, thereby helping to identify novel cellular targets to counteract cell damage in the developing human brain during metabolic failure.

RESULTS

Generation of long-term cultures of cortical brain organoid slices (cBOS)

The workflow to generate and functionally characterize cBOS includes several steps (Figure 1). First, we generated regionalized cortical organoids following our published protocol[25] which is a modified version based on the procedures introduced by Velasco and colleagues.[26] To enhance robustness, we implemented an AggreWell-based pipeline that was described by Miura and colleagues.[27] Cortical organoids were kept on an orbital shaker accompanied with subsequent media changes until 70–79 days *in vitro* (DIV, Figure 1A).

For the preparation of organoid slice cultures, we modified previous protocols published for unguided whole-brain cerebral organoids[18] and for organotypic tissue slice cultures of mouse brain.[28,29] In brief, cortical organoids were washed in Hank's balanced salt solution (HBSS) and embedded in low melting point (LMP) agarose for the preparation of acute, vital slice preparations. Agar blocks were bathed in cold HBSS and 300 μm slices were generated using a vibratome. As a modification to a procedure published earlier for unguided cerebral organoids,[18] slices were washed in pre-warmed HBSS and then placed on cell culture inserts. Visual inspections throughout the entire process ensured the integrity of the slices. The slices were immediately transferred to an incubator at 36°C at the interface between humidified carbogen (5% CO_2/95% O_2) and culture medium, and subsequently grown with daily media exchange (Figure 1B). cBOS were used for further analysis between additional 28–245 days after their generation (Figure 1C). Hereafter, the term "DIV" is referred to the total days in culture of the mentioned preparation. Hence for cBOS, DIV include the days in culture as 3D cortical organoid structures plus the days as cultured slices.

cBOS host mature neurons and astrocytes and exhibit pre- and post-synaptic markers

Cortical organoids showed an homogeneous spherical shape,[25,26] a feature that is advantageous to improve robustness and reproducibility. To study the cellular organization and maturation of cortical organoids prior to cBOS generation, we sliced 3D cortical organoids at DIV 70 in 100 μm-thick slices and labeled them for different neural markers (Figure 2).

As previously reported,[25,26,30] neural progenitors positive for paired box protein 6 (PAX6) showed an organized architecture, as seen by ring-shaped arrangements mostly devoid of cellular structures in their center, indicating the formation of ventricle-like neurogenic zones (Figure 2A, top). Beta-III tubulin (TUJ1) (Figure 2A, top & center) as well as microtubule-associated protein 2 (MAP2) staining (Figure 2A, bottom) identified neuronal cells throughout the preparation, demonstrating the presence of developing neurons. Importantly, we confirmed the presence within cortical organoids of cells positive for the transcription factor COUP TF1-interacting protein 2 (CTIP2), which is a marker of deep layer neurons within the developing cortex[18,21] (Figure 2A, bottom). We also identified GFAP-positive cells, which is a marker for astrocytes and cells of the astrocyte lineage, that mainly developed at the exterior borders of the organoids (Figure 2A, center).[31] Ultrastructural analysis by transmission electron microscopy showed elongated mitochondria containing lamellar-type cristae structures, indicating the presence of mature mitochondria (Figure 2B).

Next, we probed for the presence of prototypical synaptic proteins in cortical organoids based on synapsin 1 (SYN1) and vesicular glutamate transporter 1 (VGLUT1), which are both expressed at pre-synaptic terminals. Post-synaptic structures were visualized by labeling of HOMER1 and post-synaptic density protein 95 (PSD95). All synaptic markers were abundantly present within cortical organoids, suggesting the presence of mature synapses (Figure 2C). Taken together, the regionalized cortical organoids recruited for cBOS production exhibited both abundant neural progenitor cells and mature, synapse-bearing neurons and astrocytes, as well as the presence of CTIP2-positive deep layer neurons.

The general organization of cBOS was analyzed at DIV 98–102 (i.e., 28–32 days after their preparation from organoids). Given that the cortical organoid protocol results into homogeneous spherical organoids, cBOS had a mostly circular shape with an average diameter of about 2 mm (N = 5) at DIV 98–100. Staining with Propidium Iodide (PI), a well-established marker for assessing cell death (e.g.,[32,33]) showed that cBOS at DIV 107–116 were essentially PI-negative, exhibiting only occasional PI-positive cell bodies throughout the entire preparation (N = 3; Figure S1). In negative controls, treated with the solvent of PI only (omitting PI), untreated cBOS never displayed any label (N = 3; not illustrated). When we induced a scratch wound across a cBOS at DIV 107–116 (N = 3), PI-staining (performed 22 h after the scratch) revealed

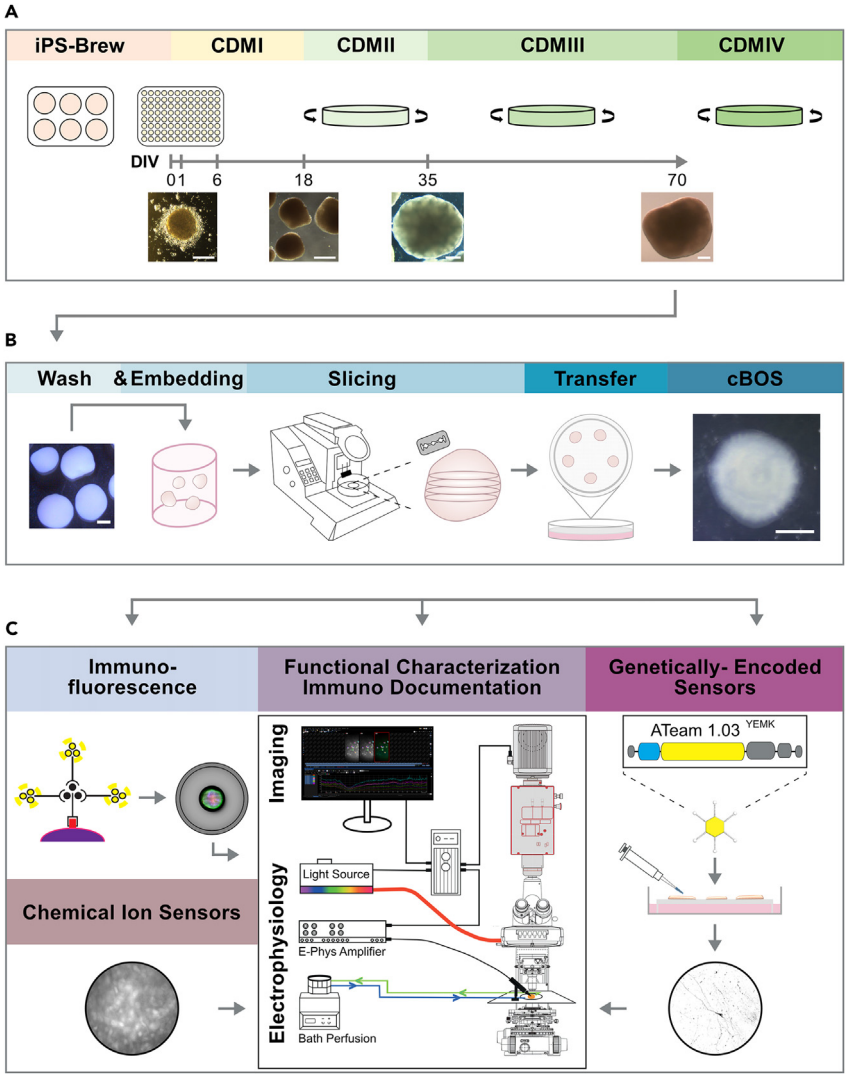

Figure 1. Generation of long-term cultures of cortical brain organoid slices (cBOS)

(A) Scheme of cortical organoid generation. iPSCs were cultured in 6-well plates in iPS-Brew medium. After detaching and dissociating cells, cell suspension was transferred into different cortical differentiation media (CDMI-IV) and cultured in 96-well plates on an orbital shaker until DIV 70–79. The photomicrographs in the bottom row show representative images at days 1, 18, 35, and 70. Scale bars, 400 μm.

(B) Scheme of cBOS preparation. Following a wash step, up to 5 cortical organoids were embedded in a block of low melting point agarose, and sliced at a precision microtome. Slices were transferred onto interface membranes in 6-well plates and cultured for up to DIV 315. Scale bars, 1 mm.

(C) Scheme of approaches for morphological and physiological characterization of cBOS. cBOS were immunohistochemically characterized (top left and center), passively loaded with a chemical ion sensor (bottom left), transduced with a genetically-encoded sensor for ATP imaging (right), or functionally characterized by electrophysiology or ion imaging (center).

the site of injury by brightly stained cells at the edge of the wound and a decreasing number of PI-positive cells toward the periphery, i.e., toward the still healthy tissue. Finally, a strong staining of the entire tissue was obtained after exposing DIV 107–116 cBOS to glucose-free ACSF, to which 2 mM 2-Deoxy-D-glucose (2-DG) and 5 mM sodium azide (NaN_3) had been added for 10 min to block cellular ATP production ("chemical ischemia") (N = 3; Figure S1). These experiments indicate the absence of regions with increased cell death in cBOS under control conditions. Nuclear staining moreover revealed a high density of cells throughout the entire preparation, again suggesting the absence of necrotic regions (Figure 3A). The same was true for cBOS maintained in culture for prolonged periods (up to DIV 315), which had grown to an average diameter of 3.5 mm (N = 4) and showed a high density of cells in their center regions (Figure 3A).

Prominent ring-shaped arrangements, presumably representing ventricle-like zones, were detected in the majority of DIV 98–102 cBOS (Figure 3A). Staining for MAP2 and TUJ1 revealed a dense network of fasciculated structures, indicative of neuronal fiber tracts in DIV 100–116 cBOS (Figures 3B and 3C). In addition, DIV 98–116 cBOS hosted a large number of S100β-positive (Figure 3B) as well as

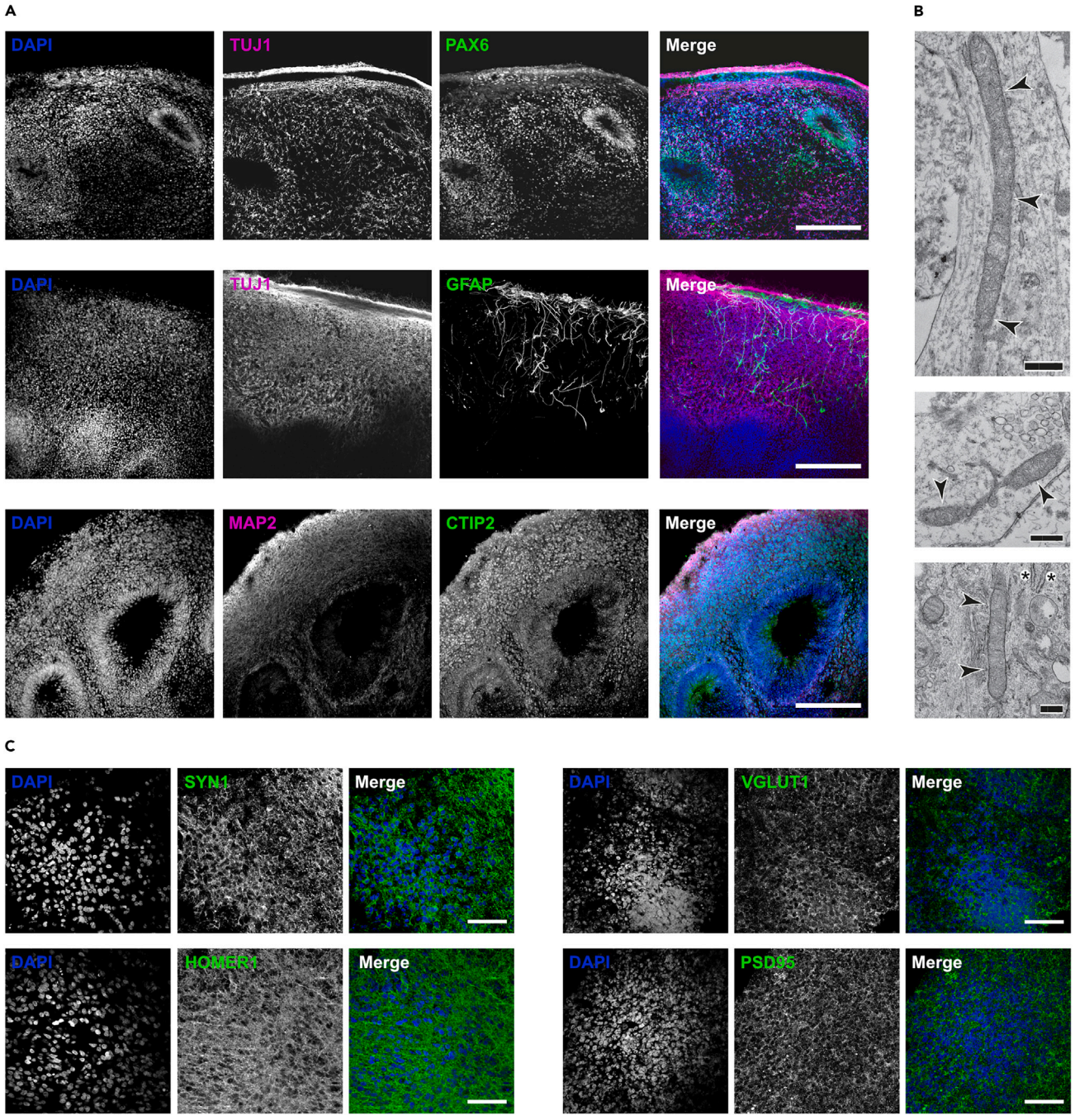

Figure 2. Cortical organoids host neural progenitors as well as mature neurons and astrocytes

(A) Top: Immunofluorescence labeling of the neuronal marker TUJ1 and the neural progenitor marker PAX6 in cortical organoids at DIV 70. Center: Double-staining for TUJ1 and GFAP, a marker for astrocytes and cells of the astrocyte lineage. Bottom: Double-staining for MAP2 (neurons) and CTIP2 (marker of deep layer neurons). Nuclei are stained with DAPI. Merge shows the overlay of three channels. Scale bars, 200 μm.

(B) Representative images from transmission electron microscopy of cortical organoids at DIV 107 show elongated mitochondria (arrows) with lamellar cristae. The endoplasmic reticulum is marked by stars. Scale bars, 500 nm.

(C) Immunofluorescence labeling for the pre-synaptic markers synapsin 1 (SYN1) and vesicular glutamate transporter 1 (VGLUT1) as well as the post-synaptic markers HOMER1 and post-synaptic density protein 95 (PSD95) in cortical organoids at DIV 70 (SYN1 and HOMER1) and at DIV 78 (VGLUT1 and PSD95). Nuclei are stained with DAPI. Merge shows the overlay of two channels. Scale bars, 50 μm.

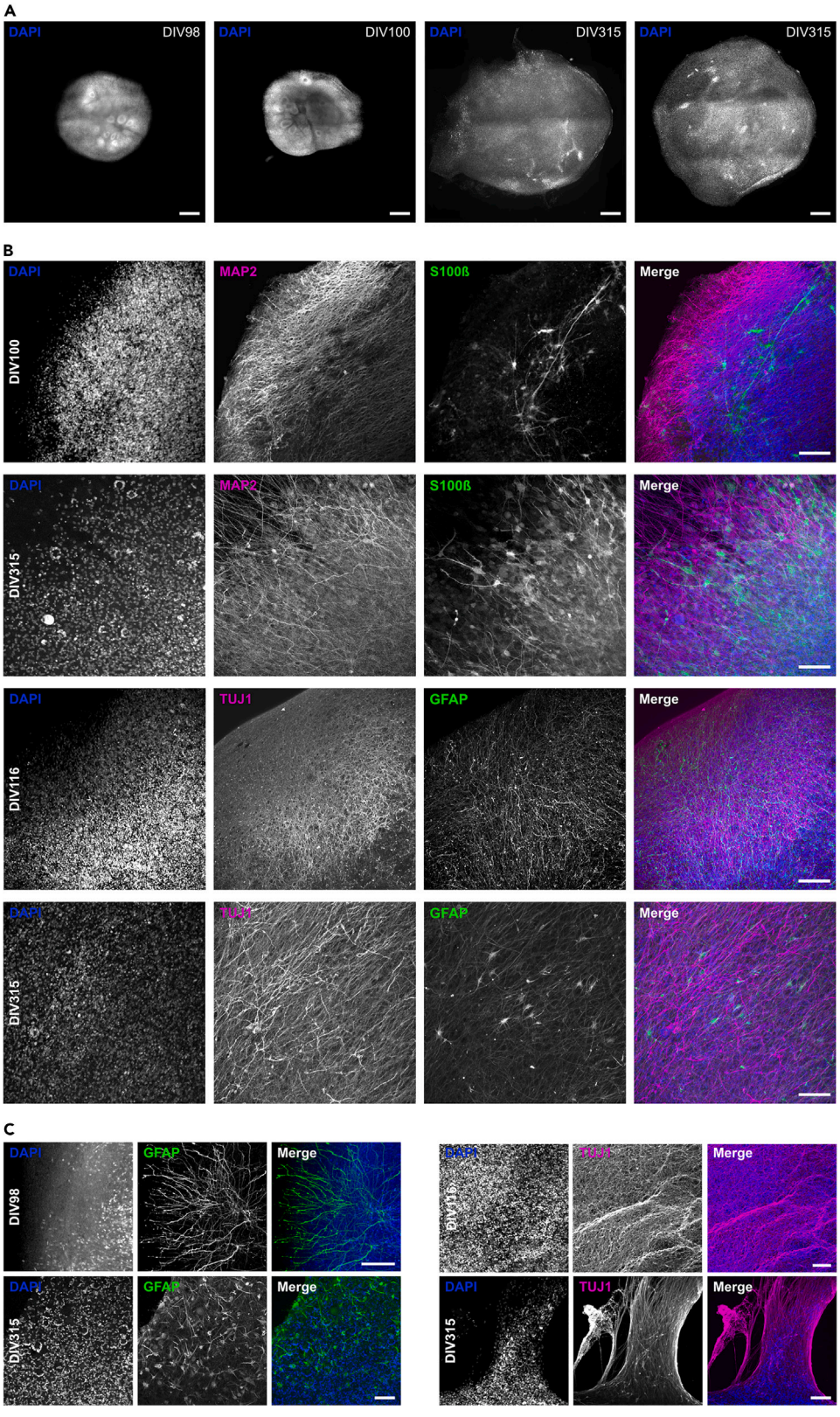
A
DAPI
DIV98
DAPI
DIV100
DAPI
DIV315
DAPI
DIV315
B
DAPI
DIV100
MAP2
S100ß
Merge
DAPI
DIV315
MAP2
S100ß
Merge
DAPI
DIV116
TUJ1
GFAP
Merge
DAPI
DIV315
TUJ1
GFAP
Merge
C
DAPI
DIV98
GFAP
Merge
DAPI
DIV315
GFAP
Merge
DAPI
DIV116
TUJ1
Merge
DAPI
DIV315
TUJ1
Merge

Figure 3. cBOS host mature neurons and astrocytes

(A) Stitched wide field images display the overall structure and size of DAPI-labeled cBOS at different DIV (DIV 98–315) as indicated. Nuclei are stained with DAPI. Scale bars, 500 μm.

(B) Representative extended-focus projections show detailed cellular organization of MAP2- and S100β-positive cells in cBOS at DIV 100 and at DIV 315 (upper two panels). The lower two panels show labels for TUJ1 and GFAP at DIV 116 and at DIV 315. Merges show the overlay of three channels. Scale bars, 100 μm.

(C) Representative extended-focus projections display details of GFAP-positive cells (left, scale bar, 100 μm) and TUJ1-positive cells (right, scale bar, 50 μm) in cBOS at DIV 98–116 and 315 respectively. Merge shows the overlay of two channels.

GFAP-positive (Figures 3B and 3C) cells, which showed a high degree of ramification of their processes, suggesting the presence of mature astrocytes. Comparable staining patterns were observed in DIV315 cBOS stained with these markers (MAP2, TUJ1, S100β & GFAP) (Figures 3B and 3C). Notably, an increase in fasciculated MAP2/TUJ1-positive structures was observed at DIV315, indicating an increase in the formation of neuronal projections and axonal tracts. In addition, areas predominantly hosting somata were found that were separated from areas with projection pathways connecting the somatic areas, suggesting functional specialization within cBOS (Figures 3B and 3C). Within the projection tracts, astrocytes were often linearly oriented along neuronal processes, similar to white matter tracts in acute brain tissue samples (not shown).

Next, we probed for the presence of prototypical synaptic proteins in cBOS using markers of pre-synaptic terminals SYN1 and VGLUT1 and of post-synaptic structures HOMER1 and PSD95 (Figure 4A). We could detect strong labeling for all synaptic markers, indicating the presence of mature synapses in cBOS. Volume-view images of MAP2-positive structures moreover indicated that dendrites were densely decorated with short (1–4 μm long) filopodial structures as well as dendritic spines, the latter characterized by the presence of a presumed spine neck and head (Figure 4B). Similarly, MAP2 staining revealed cells with a morphology typical of pyramidal neurons, including a pyramidal-shaped soma and dendrites with putative dendritic spines in DIV 315 cBOS (Figure 4C).

Taken together, these results show that cBOS derived from human cortical brain organoids exhibited ventricle-like neurogenic zones and exhibited continued cell proliferation and growth in long-term culture. Moreover, they indicate that cBOS hosted a dense network of mature, synapse-bearing (spiny) neurons as well as mature astrocytes. At about 10 months, cBOS exhibited an increase in neuronal fiber tracts and fasciculation, indicating an increase in connectivity with prolonged culturing.

cBOS host neurons which receive synaptic input and are able to generate action potentials

Immunocytochemistry revealed a dense network of MAP2-positive fibers in cBOS, suggesting the presence of mature neurons. To probe for the functional properties of those neurons, we performed electrophysiological recordings of single cells. cBOS were transferred to an experimental chamber that was constantly perfused with artificial cerebrospinal fluid (ACSF). cBOS were inspected in transmitted light, and cells that exhibited a typical neuronal morphology (oval-round cell body, at least 1–2 visible processes, bright appearance in DIC optics) were chosen and subjected to whole-cell patch-clamp. Addition of Alexa 488 to the intracellular saline enabled the online visualization of the morphology of the patch-clamped cells (Figure 5A).

Cells held in the current clamp mode had an average resting membrane potential of -51.5 $\pm$ 12.5 mV and an input resistance of 92 $\pm$ 23 MΩ under zero-current conditions (range: 50–120 MΩ; n = 11, N = 11) (Figure 5B). While membrane potentials generally slowly fluctuated by about 5–7 mV, the majority of cells (8/11 cells) additionally displayed fast sub-threshold depolarizations by 13 $\pm$ 7 mV that lasted 1–2 s (Figure 5C). 2 of 11 cells recorded from also displayed spontaneous action potentials that showed an overshoot to about +30 mV after which the membrane potential recovered toward its initial resting value without a clear undershoot (Figure 5D). Addition of tetrodotoxin (TTX, 0.5 μM) to the ACSF to block voltage-gated Na^+ channels strongly dampened the minor fluctuations in the membrane potential (in 3 out of 4 cells); moreover, fast sub-threshold depolarizations were absent and action potentials never observed (n = 4, N = 4) (Figure 5E).

Analogous behavior was observed when cells were held in the voltage clamp mode (n = 6, N = 6) (Figure 5F). In control conditions, 5/6 cells showed slow current fluctuations in addition to frequent fast inward currents at an average peak amplitude of 19 $\pm$ 7 pA, occurring as singular events or in a burst-like manner. Both slow fluctuations as well as fast inward currents were absent in the presence of TTX in 3 out of 4 cells (Figure 5G). When subjected to a rectangular, stepwise current injection protocol (from −90 to +260 pA in increments of 50 pA applied for 500 ms), cells showed large, slowly developing hyperpolarizations with negative current injections (Figure 5H). In 5 out of 11 cells, an initial action potential was triggered with positive current injection, that was followed by a second, broad and low-peak action potential for higher depolarizing currents (n = 11, N = 11) (Figure 5H). Application of TTX abolished the generation of initial fast action potentials (n = 3, N = 3) (Figure 5I).

In summary, these results indicate that cBOS host mature neurons which express functional TTX-sensitive voltage-gated sodium channels and are capable of generating action potentials. Moreover, they indicate pre-synaptic, action-potential-dependent release of transmitters, as well as vivid post-synaptic input and synaptic communication between neurons.

cBOS display spontaneous and evoked network calcium signaling

Intracellular calcium signaling is a reliable reporter of neural activity. We performed multi-cell bolus-loading of the chemical calcium indicator Oregon Green BAPTA-1-A.M. (OGB-1-AM) in cBOS which enabled imaging of intracellular calcium in essentially the entire cellular network in the field of view (Figure 6A). At physiological temperature (37 $\pm$ 1°C), about half (48%) of the cells recorded from exhibited spontaneous somatic calcium signals (n = 56/116 cells, N = 5) (Figures 6B and 6C). Signals were usually not synchronized between cells. The percentage of spontaneously active cells dropped to 21% when cBOS were perfused with TTX (n = 11/53 cells, N = 3) (Figures 6B and 6C). Results obtained at

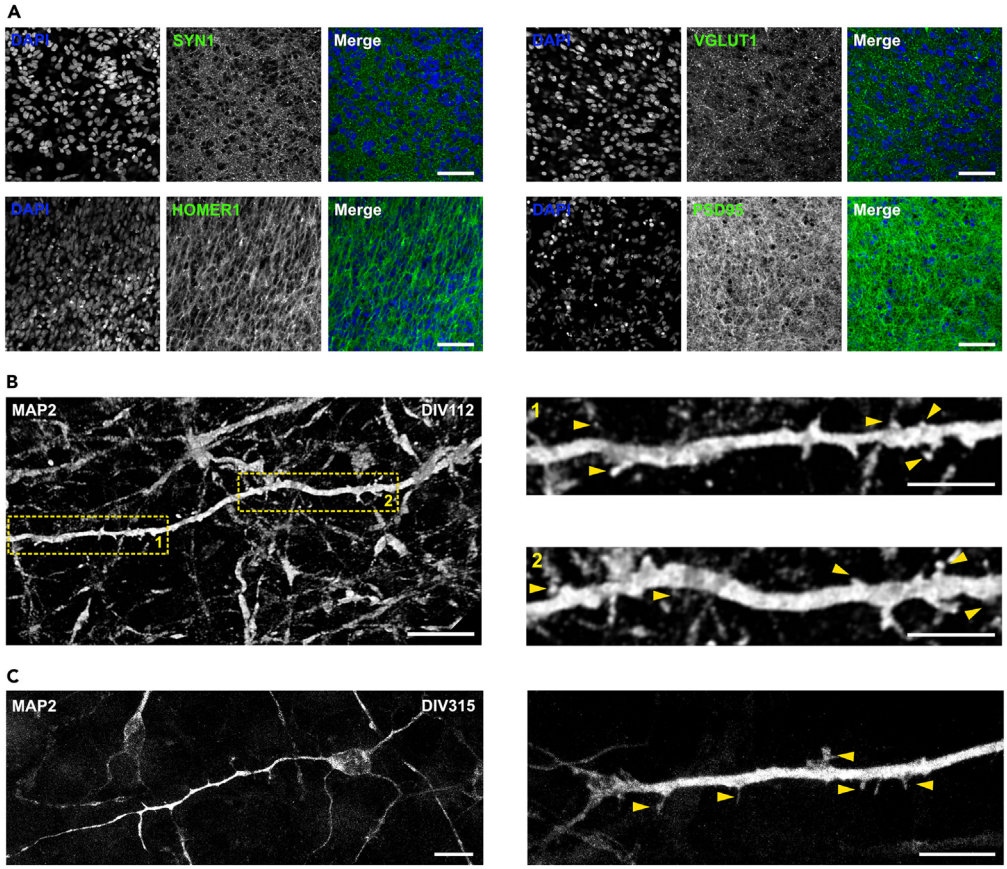

Figure 4. cBOS exhibit pre- and post-synaptic markers and presumed dendritic spines

(A) Immunofluorescence labeling for the pre-synaptic markers SYN1 and 'VGLUT1 and the post-synaptic markers HOMER1 and PSD95 in cBOS DIV 125. Nuclei are stained with DAPI. Merge shows the overlay of two channels. Scale bars, 50 μm.

(B) Volume-view snapshot showing neuronal morphology in more detail (dendrites, MAP2-positive) in cBOS at DIV 112 (Scale bar, 15 μm). Note filopodial structures and presumed dendritic spines characterized by structures reminiscent of spine necks and heads (yellow triangles). Magnifications are shown in blow ups (B1 & B2). Scale bars, 5 μm.

(C) Representative extended-focus projections reveal the presence of neurons with pyramidal-shaped cell bodies and spiny dendrites in DIV 315 cBOS. Scale bars, 50 μm (left) and 5 μm (right).

room temperature (22 ± 1°C) showed slightly reduced activity; roughly 20% of the cells showed spontaneous calcium transients (n = 54/344, N = 5; not shown).

To foster network activity, cBOS were perfused with a modified ACSF at 37°C, which was devoid of Mg^{2+} to unblock ionotropic NMDA receptors and contained 10 μM bicuculline methiodide, a $GABA_A$ receptor antagonist. This protocol has been widely used to induce glutamate-driven recurrent bursting behavior in acute slices of the juvenile rodent hippocampus.[34] Several minutes after wash-in, synchronized and large-scale network calcium activity was observed, involving all cells in the field of view (n = 94, N = 4) (Figure 6D). Signals were long-lasting (about 10–30 s) and often grouped in bursts consisting of several individual calcium signals (Figure 6D, inset).

Based on these findings, we probed for the presence of ionotropic glutamate receptors in cBOS. Bath application of glutamate (10 s/1 mM) reliably induced calcium signals in all cells recorded from, exhibiting an average relative increase in fluorescence of 13.0 ± 8.8% (n = 172, N = 6) (Figures 6E and 6F). Upon wash-in of the NMDA receptor blocker APV (100 μM), the peak amplitude of glutamate-evoked calcium signals was strongly dampened (to 4.1 ± 3.0%; n = 110, N = 3; p = 0.000, ***). Subsequent combined application of APV and the AMPA-receptor blocker NBQX (50 μM) resulted in a slight increase in the mean amplitude as compared to application of APV alone (4.5 ± 3.7%; n = 104, N = 3; p = 0.000, ***) (Figures 6E and 6F). Finally, we bath applied GABA (10 s/1 mM), which induced small calcium signals with an average amplitude of 4.2 ± 4.6% in the vast majority of cells analyzed (35/37 cells, N = 3; not shown). In the presence of the $GABA_A$ receptor blocker bicuculline methiodide, the number of cells responding to GABA with an increase in calcium was strongly reduced (26/47 cells, N = 3; not shown).

Taken together, these results demonstrate that cBOS show spontaneous and evoked calcium signaling. The data is in agreement with the observation that cells within cBOS exhibit functional voltage-gated sodium channels and exhibit spontaneous action potential-related activity, which will promote intracellular calcium signaling. Our findings moreover provide evidence for the expression of ionotropic NMDA as well

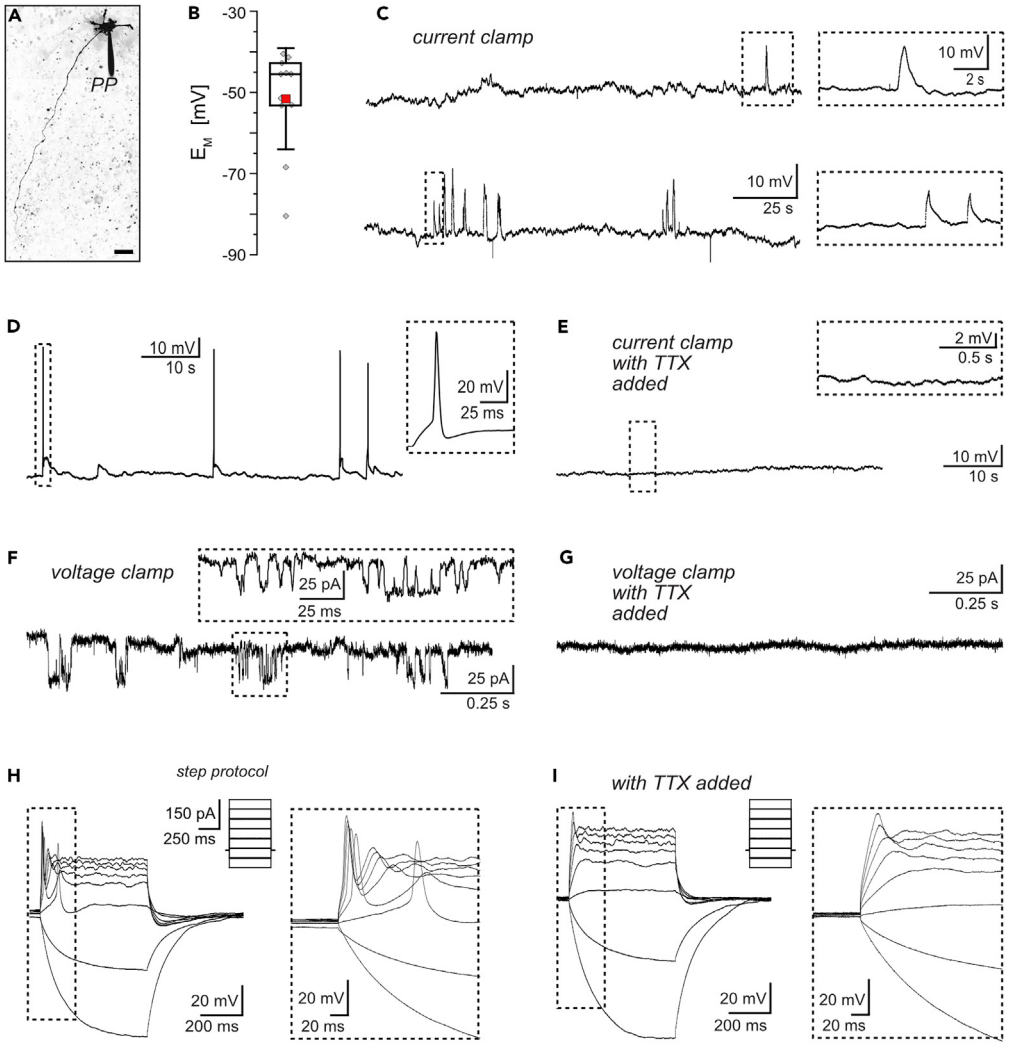

Figure 5. cBOS host neurons which receive synaptic input and are able to generate action potentials

(A) Multi-photon image of a cell filled with Alexa 488 through a patch pipette (PP) in a cBOS at DIV 114. Image was inverted for illustration purposes. Scale bar, 10 μm.

(B) Boxplot illustrating the membrane potential of cells as determined by current clamp recordings. Shown are mean (red square), median (black line), 25/75 percentiles (box), 1x SD (whiskers) and single data points (gray diamonds). Number of cells: 11, number of slices: 11.

(C) Recordings of the membrane potential of two different cells held in current clamp. Inserts display blow-ups of traces to illustrate large subthreshold depolarization events.

(D) Current clamp recording showing spontaneously generated action potentials. Inset illustrates action potential at higher temporal resolution.

(E) Current clamp recording in the presence of TTX.

(F) Voltage-clamp recording showing spontaneous fast inward currents. Inset illustrates current at higher temporal resolution.

(G) Voltage-clamp recording in the presence of TTX.

(H) Current clamp recording of a neuron subjected to a rectangular, stepwise current injection protocol (−90 pA to +260 pA in increments of 50 pA as indicated). Inset illustrates initial phase of current injection at higher temporal resolution.

(I) Current clamp recording of a neuron subjected to a rectangular, stepwise current injection protocol in the presence of TTX. Inset illustrates initial phase of current injection at higher temporal resolution.

as $GABA_A$ receptors within cBOS. Thus, cBOS contain a network of highly coupled cells capable of generating large-scale recurrent excitatory network activity.

Chemical ischemia causes calcium loading and a decline in intracellular ATP in cBOS

The brain has exceptionally high energy needs and requires the constant production of cellular adenosine triphosphate (ATP). Failure of energy metabolism therefore leads to rapid functional failure and cell death of neurons as observed in human stroke.[35,36] Moreover, effective

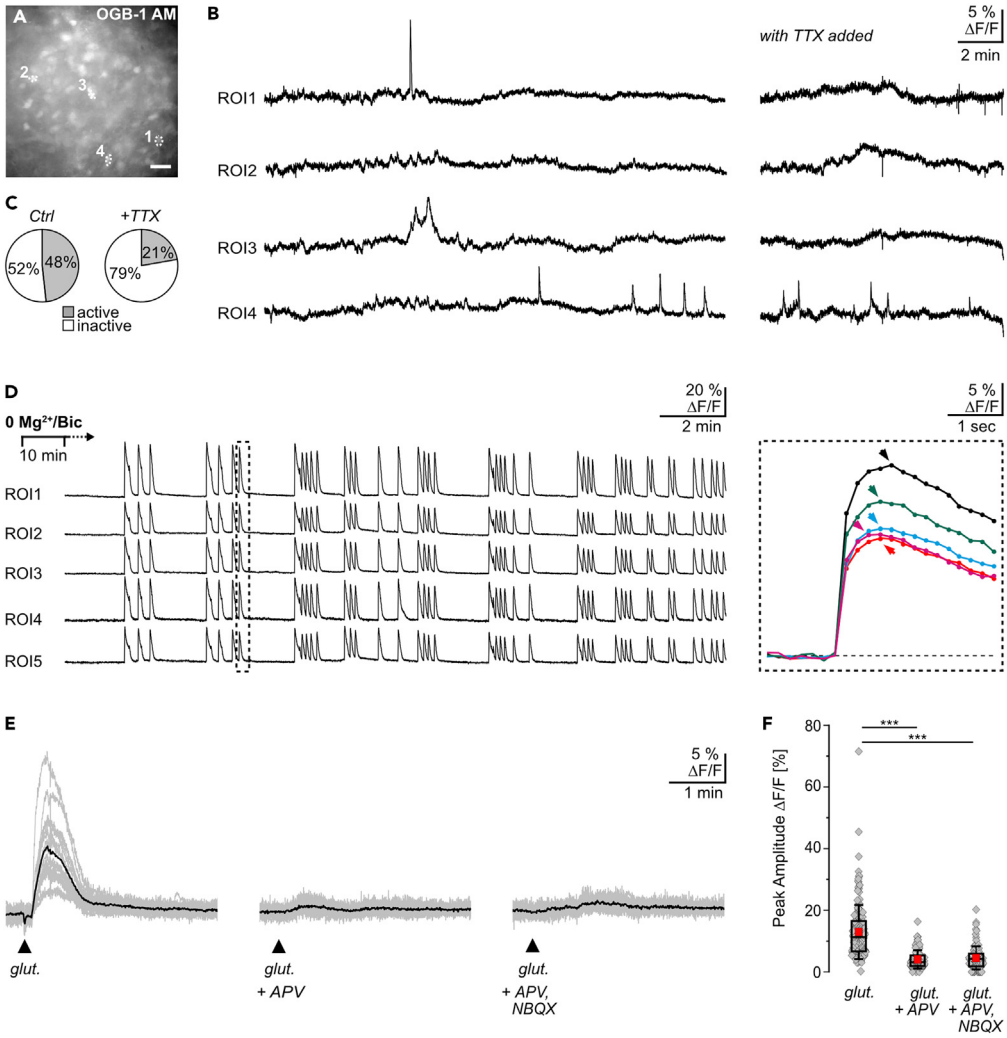

Figure 6. cBOS display spontaneous and evoked network calcium signaling

(A) Wide field image (MIP of first 5 frames) of an OGB-1-AM loaded cBOS at DIV 147. Dashed lines indicate regions of interest (ROIs) 1–4 depicted in (B). Scale bar, 25 μm.

(B) Spontaneous changes in intracellular calcium in ROIs 1–4 in control condition (left) and in the presence of TTX (right).

(C) Percentage of active vs. inactive cells in control condition (Ctrl) and presence of TTX.

(D) Synchronous network calcium oscillations in 5 different cells (ROIs 1–5) induced by perfusion with Mg^{2+}-free ACSF containing 10 μM of the $GABA_A$ receptor antagonist bicuculline methiodide (0 Mg^{2+}/Bic), washed in 10 min before. The inset on the right shows the period indicated with the dotted box at higher temporal resolution. Note that even at the low temporal resolution of the imaging experiments (5 Hz), differences in the kinetics of calcium transients can be detected between individual cells, e.g., different time points of their maximum peaks.

(E) Changes in calcium in a cBOS at DIV 99 in response to bathe application of 1 mM glutamate (glut.) for 10 s as indicated by the arrowheads. Left: control; middle: upon wash-in of the NMDA receptor blocker APV (100 μM); right: upon wash-in of APV and the AMPA receptor blocker NBQX (50 μM). Illustrated are individual traces of 22 cells (gray) recorded in a single experiment and the corresponding average trace (black).

(F) Boxplots illustrating the peak amplitude of glutamate-induced calcium transients in control (glut.) and with blockers as indicated. Shown are means (red squares), medians (black lines), 25/75 percentiles (boxes), 1x SD (whiskers) and single data points (gray diamonds). Glut: Number of cells: 172, number of slices: 6; Glut. + APV: Number of cells: 110, number of slices: 3; Glut. + APV + NBQX: Number of cells: 104, number of slices: 3. ***$p < 0.001$; not significant: $p \geq 0.05$. For statistical evaluation, data were analyzed by a Kolmogorov-Smirnov normality test. Non parametric data were tested via Mann-Whitney U test.

mitochondrial metabolism is central for neuronal development and for ensuring resilience against neurodegenerative diseases.[37,38] We used cBOS to study the dependence of human cortical cells embedded in a functional network on an intact energy metabolism.

Animal models have shown that calcium overload is a major trigger of cell death in ischemic stroke.[35,36] Here we tested if ischemic conditions also induce calcium increases in human cBOS. To this end, cBOS were loaded with OGB-1-AM and subjected to pharmacological inhibition of glycolysis and oxidative phosphorylation ("chemical ischemia"; see above). Perfusion with the metabolic inhibitors for 2 min

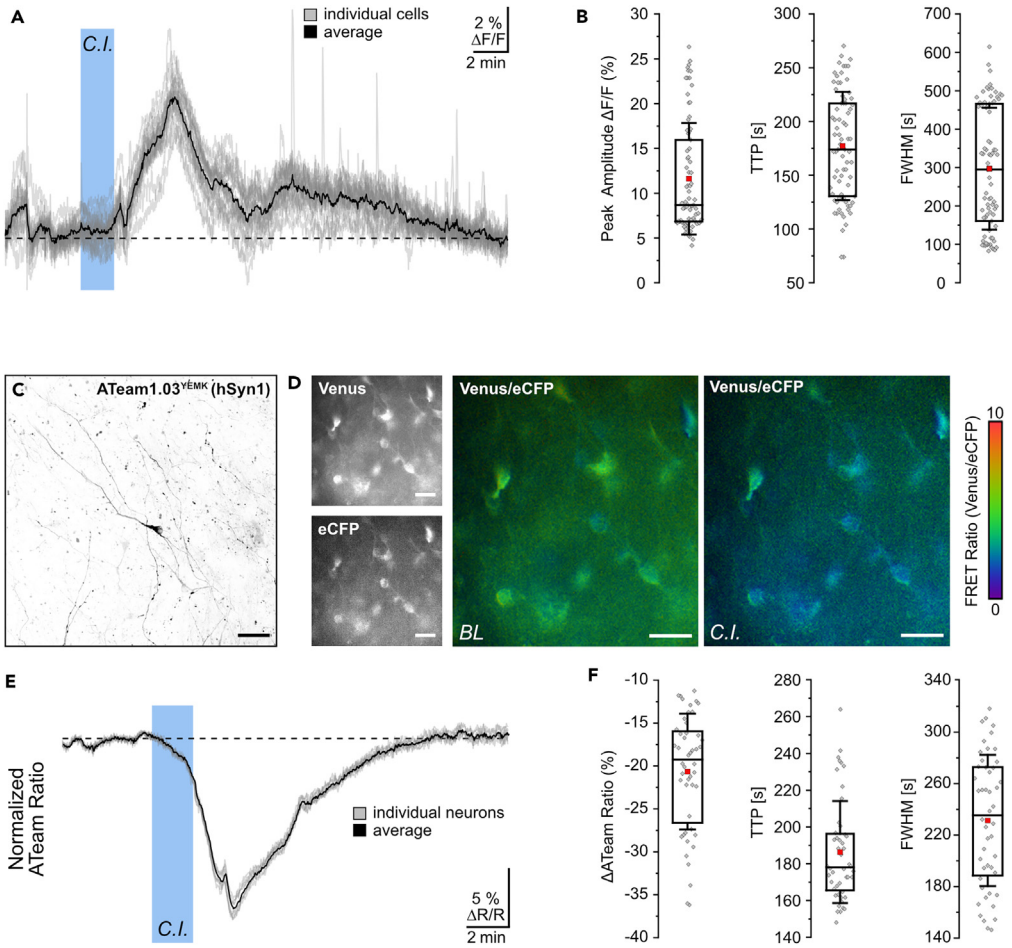

Figure 7. Chemical ischemia causes calcium loading and a decline in intracellular ATP in cBOS

(A) Change in intracellular calcium in a cBOS at DIV 102 induced by a 2-min period of chemical ischemia (blue area). Illustrated are individual traces (21 cells, gray) and the corresponding average trace (black).

(B) Boxplots illustrating the peak amplitude of calcium transients induced by chemical ischemia. Shown are means (red squares), medians (black lines), 25/75 percentiles (boxes), 1x SD (whiskers) and single data points (gray diamonds). Number of cells: 77, number of slices: 5.

(C) Confocal image of ATeam1.03^{YEMK}-transduced neurons (excited at 488 nm), expressed under the control of the human synapsin 1 (hSyn1) promotor. Image was inverted for visualization purposes. Scale bar, 25 μm.

(D) Left: Wide field images of fluorescence emission (top: Venus/527 nm; bottom: eCFP/475 nm) of neurons expressing ATeam1.03^{YEMK}. Center & Right: Wide field images of the fluorescence ratio of Venus/eCFP at baseline level (BL) and during chemical ischemia (C.I.). Colored scale bar indicates ATeam1.03^{YEMK} ratio with blue representing low and red representing high values. Scale bars, 25 μm.

(E) Relative changes in the ATeam1.03^{YEMK} ratio of 8 neurons in a cBOS at DIV 120 induced by a 2-min period of chemical ischemia (blue area). Illustrated are individual traces (gray) and the corresponding average trace (black).

(F) Boxplots illustrating relative changes in the ATeam1.03^{YEMK} ratio induced by chemical ischemia. Shown are means (red squares), medians (black lines), 25/75 percentiles (boxes) and 1x SD (whiskers) and single data points (gray diamonds). Number of cells: 48, number of slices: 7. Left: peak changes in the ATeam1.03^{YEMK} ratio; center: time to peak (TTP); right: full width half maximum (FWHM).

resulted in a long-lasting increase in the intracellular calcium concentration in cBOS (Figure 7A). On average, induction of chemical ischemia caused an average relative increase in OGB-1 fluorescence by 11.6 ± 6.2%, the peak of which was reached after 177 ± 50 s and which showed a full width at half maximum of 297 ± 159 s (n = 77, N = 5) (Figure 7B).

To investigate the cellular consequences of brief chemical ischemia on cellular ATP levels, we expressed the genetically-encoded, FRET-based nanosensor ATeam1.03^{YEMK} (ATeam) under the control of the human synapsin 1 (hSyn1) promotor, allowing us to perform quantitative imaging of changes in neuronal ATP. Cells transduced with ATeam exhibited typical neuronal morphologies, with pyramidal-shaped to oval cell bodies from which several long and thin ramifying processes extended (Figures 7C and 7D). Chemical ischemia for 2 min caused an immediate decrease in the ATeam ratio by 20.7 ± 6.7% which was reached after 186 ± 28 s and exhibited a full width at half maximum of 231 ± 51 s (Figures 7E and 7F). ATP levels recovered to levels close to the initial baseline within about 12 min (n = 48, N = 7) (Figure 7E).

These results thus demonstrate that cBOS are highly sensitive to inhibition of the main metabolic pathways for ATP production, implying high cellular energy needs. They show that inhibition of glycolytic and mitochondrial ATP production leads to a rapid increase in intracellular calcium concentrations in human cBOS, accompanied by an immediate decrease in intracellular ATP.

DISCUSSION

In the present work, we describe the characteristics of cBOS obtained from regionalized cortical organoids derived from human pluripotent stem cells (hPSCs). Human brain organoids from hPSCs represent a powerful tool to study human neurodevelopment as they reproduce several key steps of neural maturation.[9,11] However, with their continued growth in culture conditions, their sophisticated 3D structure also may inherit hypoxic/ischemic conditions and insufficient nutrient supply to their inner core, resulting in cell death and restricted cellular differentiation.[16,17,39] To improve cellular energy supply, brain organoids can be grown in spinning bioreactors,[16] but necrotic cores may still develop over time.[17] Different approaches have thus been attempted, including assembly with endothelial cells to increase vascularization, and grafting of brain organoids into mouse brain.[40–42] Such approaches are usually low throughput and, owing to their complexity, not yet readily applicable to all laboratories. In addition to maturation aspects, the structure of large-diameter 3D brain organoids complicates the direct probing of neuronal functionality. The specific targeting and live-cell analysis of neural cells in layers well below the surface can be challenging and may require sophisticated technical approaches such as multiphoton- or multidimensional light-sheet imaging or Neuropixels probes.[23,43–46] Some of the above mentioned limitations related to maturation and functionality may be circumvented by preparation of acute slices or the dissociation and subsequent culturing of cells from human brain organoids, facilitating investigation of functional cellular properties.[8] Nonetheless, acute slices do not prevent the presence of a necrotic core in developing 3D organoids and are viable for a few hours only.

Cultures of sliced air-liquid interphase cerebral organoids (ALI-COs) can solve some of these issues. They have been generated starting from whole-brain cerebral organoids.[16,18,19] More recent approaches guided the 3D differentiation toward region-specific identities for establishment of cortical organoids, striatal organoids, midbrain organoids and many more.[43,47] Such patterned and regionalized brain organoids appear to be more homogeneous and robust,[26] and can also be used to study the interplay between different brain regions through the assembly *in vitro* of different regionalized brain organoids.[48] Compared to 3D brain organoids, slices from brain organoids kept in long-term culture show reduced cell death in the central region and improved growth and cellular maturation.[18,20,21] A clear disadvantage of organoid slices is the reduction in tissue complexity and the loss of a larger 3D structure combined with the loss of already established connections and a necessary re-organization of the tissue. In that sense, organoid slices show less resemblance and comparability to the developing human brain.

An important advantage of sliced organoids is that they enable a more direct access to the tissue. This aspect can facilitate the implementation of multi-electrode array recordings for measurement of extracellular field potentials and neuronal spiking activity.[18,21,23,24] Importantly, cultured organoid slices also enable better standardization and comparability of experimental results because multiple slices can be derived from the same organoid and further employed in downstream assays for drug screening or disease modeling applications. In the present study, we utilized these advantages of organoid slices. Our results show that cBOS at DIV 107–116 were essentially PI-negative, suggesting negligible cell death at this culturing stage. cBOS could be kept for extensive culture on an the air-liquid interface. Even with prolonged culturing, cBOS maintained a high labeling density and fluent labeling for DAPI throughout the entire preparation including the center regions, suggesting the lack of massive cell death as often found in the inner core parts of older brain organoids cultured in 3D.[16–18,21]

As observed for their "parent" cortical organoids, DAPI staining indicated the presence of ventricle-like zones in cBOS. In addition, dense labels for neuronal structures (MAP2-positive) were found, implying the presence of mature neurons. MAP2 immunolabelling also indicated a fasciculation and formation of neuronal fiber tracts in addition to filopodia and spine-like structures along dendrites. Different pre- and post-synaptic markers, including PSD95 and VGLUT1 for glutamatergic synapses, revealed the presence of mature chemical synapses. Notably, at DIV >300, cBOS exhibited an increased fasciculation of neuronal fiber tracts as compared to about 3–4 months in culture, indicating increased formation of axonal projections and increased connectivity. cBOS moreover hosted S100β- and GFAP-positive cells with a high degree of ramification, demonstrating the presence of cells of the astrocyte lineage as well as of mature astrocytes, which are essential for fully functional neuronal activity. Hence, we conclude that cBOS can develop to an intact, synaptically connected neural network hosting mature neurons and astrocytes.[12,18,21,23,24]

While we did not probe for cells of the oligodendrocyte lineage, it is known from previous studies that the maturation of oligodendrocytes in brain organoids is a rather lengthy and non-efficient process. In line with this, earlier work performed in cultured slice preparations prepared from cerebral or forebrain organoids mostly identified cells of the oligodendrocyte lineage and/or precursor cells even at prolonged times in culture.[20,21] Several laboratories have therefore developed specific protocols to promote their differentiation from OPCs and to induce the production of myelin.[49–52]

We also employed cBOS for an array of functional experiments. By performing whole-cell patch-clamp recordings from individual neurons, we found frequent spontaneous inward currents as well and vivid, sub-threshold depolarizing potentials. Both forms of activity were dampened upon blocking voltage-gated Na^+ channels with TTX, indicative that they originated from weak (subthreshold) excitatory synaptic inputs. Injection of depolarizing current resulted in the generation of action potentials, again a signature of functional neurons. Moreover, some neurons showed spontaneous action potential generation, which is in line with earlier MEA recordings reporting spontaneous spiking in human brain organoids as well as in cultured organoid slices.[12,18,21,23,24,43,53,54]

Imaging experiments revealed analogous spontaneous calcium transients. We found that about 50% of cells within cBOS exhibited irregular calcium signals, which were dampened by perfusion with TTX, indicating their dependence on action potential activity. Spontaneous Ca^{2+} signaling was also reported from different preparations of whole brain organoids, neurons dissociated from them, or cultured organoid slices (e.g.,[7,8,22,44,49,55]) indicating that cells in cBOS exhibit repeated, transient phases of activity.

Besides spontaneous calcium signaling, all cBOS cells recorded showed large, APV-sensitive increases in calcium upon bath perfusion of 1 mM glutamate, indicating the expression of ionotropic NMDA receptors as found for human cortical spheroids.[56] A similar observation was made upon application of 1 mM GABA, albeit signals were much smaller and a minority of cells (2 out of 37) did not respond. In the majority of cells, GABA-induced calcium increases were blocked upon perfusion with bicuculline methiodide, indicating that they were mediated by $GABA_A$ receptor activation. Notably, while glutamatergic neurons are generally the most abundant cell type in human brain organoids, several studies also demonstrated the presence of interneurons and of GABAergic synapses, respectively.[9,18,57,58] In line with these results, disinhibition of NMDA receptors by perfusing slices with magnesium-free saline while blocking $GABA_A$-receptors turned the irregular calcium spiking pattern seen in about half of the cells into large, synchronous bursts of calcium signaling in all cells recorded from. This result indicates that essentially all cells of the cBOS network are already well-connected at this time point and capable of generating large-scale coordinated activity. In acute slice preparations from rodent hippocampus, the latter approach has been employed routinely to evoke highly synchronous epileptiform discharges.[59–61] Electrophysiological recordings showed that in the latter preparation, the excitation usually arises in one region of the preparation and then within 10–20 ms travels to neighboring areas.[59,62] Notably, even with electrodes separated by 150 μm, epileptiform activity was thus synchronous in all electrodes within a time window of 30 ms.[59] Our calcium imaging experiments in cBOS were performed at 5 Hz, and cells therefore seemingly react identically independent from the location of their cell body (a phenomenon also observed e.g., in the immature cortex, see[63]).

Synchronized bursting activity and oscillatory network events are a hallmark of organoid preparations, usually developing from spontaneous irregular patterns after several months of growth.[12,44,64,65] This recurrent activity is reminiscent of spontaneous early network calcium oscillations of neonatal rodent forebrain.[15,66] Coordinated, experience-independent patterns of synchronized spontaneous activity were also detected in the developing human brain *in utero* or in preterm human neonate brain, where they have been proposed to shape the development of neuronal networks.[12,67]

In the newborn, hypoxic-ischemic periods and the resulting decline in the cells' capacity for ATP production are a major cause of neurological disabilities.[68] Moreover, physiological mitochondrial metabolism is emerging as important regulator of early neurogenesis and may set the species-specific temporality of neurodevelopmental processes.[13,38,69,70] New treatment strategies are desperately needed to limit damage to the developing human brain caused by ischemia and energy deprivation.[68] Brain organoids have recently been proposed to fill this gap and to allow new insights into the molecular mechanisms of ischemia-induced injury.[14,33,71] The development of a necrotic core in brain organoids may, however, alter the expression of mitochondrial genes for oxidative phosphorylation.[17]

In the present study, we used cBOS to study the functional consequences of a failure of energy metabolism. To the best of our knowledge, our data show for the first time that inhibition of glycolytic and mitochondrial ATP production leads to an immediate decrease in intracellular ATP in human cortical cells embedded in a functional minimal network. Upon subjecting cBOS to 2 min of chemical ischemia, the ATeam ratio decreased by about 20%. Assuming an intracellular baseline ATP concentration of 2.5 mM, and based on our earlier *in situ*-calibrations,[29,72] this corresponds to a decline in ATP by about 0.11 mM. The latter is less than half of that observed upon the same manipulation in neurons of organotypic slices of the mouse neocortex,[73] suggesting a moderate ATP consumption of cBOS neurons under these conditions. Notably, cBOS neurons readily recovered close to their initial ATP levels upon wash-out of the drugs, indicating re-installment of efficient ATP production. This indicates that cBOS neurons can well withstand transient metabolic stress and are not in a functionally impaired metabolic state as suggested for some organoid protocols.[17,74] Chemical ischemia also induced a rapid increase in intracellular calcium concentrations in human cBOS, a finding that had not been reported before. Animal models have shown that calcium overload is a major trigger of cell death in ischemic stroke,[35,36] and based on our results, we propose that ischemia-induced calcium accumulation may also be a highly relevant trigger of cell damage in the ischemic human brain.

In conclusion, our results show that cBOS represent well-accessible networks of human-derived cortical tissue in controlled culture conditions, which are functionally active, synaptically connected, and capable of generating large-scale coordinated network activity. Their limited thickness, good technical and experimental accessibility, as well as their robustness and ease of handling make them an ideal tool for morphological and functional analyses employing techniques such as multiple- or single-cell electrophysiology or standard fluorescence imaging. Importantly, cBOS also represent a system with increased standardization and comparability as multiple slices can be derived from the same brain organoid and further employed in downstream assays for drug screening or disease modeling applications. Our results also show that cBOS will enable the study of the molecular pathways that drive cellular damage caused by hypoxic-ischemic conditions. The identification of potential new therapeutic targets in cBOS promises to improve the translation of these findings to the developing human brain to ameliorate ischemia-related neurological complications and dysfunction.

Limitations of the study

In addition to the potential pitfalls of generating cultured slice preparations from brain organoids described above, the limitations of the study relate to the intrinsic properties of current experimental procedures to generate brain organoids. These preparations are limited owing to the restricted time they can be kept in culture, and are thus mostly regarded as a model system for the study brain development.[3,9] The same holds true for cBOS introduced here. While we kept these preparations for more than 300 days, this is still a rather

restricted period when compared to human brain development and maturation. Moreover, while human brain organoids are now widely used to study the properties of human brain networks, they typically consist of cells belonging to the neuro-ectodermal lineage and their lack of intrinsic vascularization and microglia are still main limitations.[42,75] Hence, also the cBOS described here cannot be used to address aspects related to blood-brain barrier or microglial function/dysfunction. Several groups are working on strategies to incorporate endodermal-derived blood vessel cells and mesodermal-derived microglia. The presence of vasculature structure is not only crucial for distributing oxygen and nutrients throughout the organoids but also to enhance organoid maturation, as vasculature is known to play a role in enabling effective neuronal commitment and maturation *in vivo*.[39] Similarly, the incorporation of microglia into brain organoids would not only provide support for the neuronal development as shown by Park and co-workers (e.g.,[76]) but may also help unveiling the impact of immune-mediated mechanisms in the modeled diseases. In fact, xenotransplanted organoid models have been proposed to study *in vivo* human microglia derived from erythromyeloid progenitors.[77] Development of brain organoid approaches containing these cell types[24,77] would therefore be highly beneficial, and the use of cBOS in these contexts could further improve maturation and accessibility to functional neural networks.

STAR★METHODS

Detailed methods are provided in the online version of this paper and include the following:

- KEY RESOURCES TABLE
- RESOURCE AVAILABILITY
  - Lead contact
  - Materials availability
  - Data and code availability
- EXPERIMENTAL MODEL AND STUDY PARTICIPANT DETAILS
  - Cell lines
  - Human iPSC culture
- METHOD DETAILS
  - Generation of cortical brain organoids from human iPSC culture
  - Immunohistochemistry of organoids
  - Electron microscopy
  - Generation of cortical brain organoid slices
  - Immunofluorescence staining and documentation of immunolabelled cBOS
  - Propidium iodide nucleic acid stain
  - Whole-cell patch-clamp recordings
  - Imaging of intracellular calcium
  - Imaging of intracellular ATP
  - Image processing and preparation of figures
- QUANTIFICATION AND STATISTICAL ANALYSIS

SUPPLEMENTAL INFORMATION

Supplemental information can be found online at https://doi.org/10.1016/j.isci.2024.109415.

ACKNOWLEDGMENTS

The authors thank S. Durry and C. Roderigo (Institute of Neurobiology, Heinrich Heine University Duesseldorf) for excellent technical assistance. This study was supported by the German Research Foundation (DFG), Research Unit RU2795: "Synapses under stress" (RA: AN 1440/4-1; AP: PR1527/6-1; CRR: Ro2327/13-2), the European Joint Program for Rare Diseases (EJPRD) and German Federal Ministry of Education and Research (BMBF) (AP: 01GM2002A), the Leigh Syndrome International Consortium (LSIC to A.P.), People Against Leigh syndrome (PALS to A.P.), CureMito Foundation (to A.P.), the European Commission's Horizon Europe Programme (SIMPATHIC #101080249 to A.P.), the Fondation Maladies Rares (to A.P.), and Jürgen Manchot Stiftung (to S.H.). Electron microscopy was performed at the Core Facility For Electron Microscopy (CFEM) at the medical faculty of the Heinrich Heine University Duesseldorf. Authors thank Andrea Borchardt for her technical assistance in electron microscopy.

AUTHOR CONTRIBUTIONS

Conceptualization: A.P., C.R.R., K.W.K., and L.P.; Methodology, L.P., S.L., S.H., K.W.K., and R.A.; Formal Analysis: L.P., K.W.K., J.N., R.A., and L.N.; Investigation, L.P., S.H., K.W.K., J.N., and L.N.; Writing – Original Draft, L.P., K.W.K., A.P., and C.R.R.; Writing – Review and Editing, L.P., K.W.K., S.L., S.H., J.N., L.N., R.A., A.P., and C.R.R.; Funding Acquisition, R.A., A.P., and C.R.R.; Supervision, A.P. and C.R.R. All co-authors approved the final manuscript.

DECLARATION OF INTERESTS

The authors declare no competing interests.

Received: August 8, 2023
Revised: January 29, 2024
Accepted: February 29, 2024
Published: March 4, 2024

REFERENCES

1. McRae, J.F., Clayton, S., Fitzgerald, T.W., Kaplanis, J., Prigmore, E., Rajan, D., Sifrim, A., Aitken, S., Akawi, N., Alvi, M., et al. (2017). Prevalence and architecture of de novo mutations in developmental disorders. Nature *542*, 433–438. https://doi.org/10.1038/nature21062.
2. GBD 2016 Stroke Collaborators (2019). Global, regional, and national burden of stroke, 1990-2016: a systematic analysis for the Global Burden of Disease Study 2016. Lancet Neurol. *18*, 439–458. https://doi.org/10.1016/S1474-4422(19)30034-1.
3. Eichmüller, O.L., and Knoblich, J.A. (2022). Human cerebral organoids — a new tool for clinical neurology research. Nat. Rev. Neurol. *18*, 661–680. https://doi.org/10.1038/s41582-022-00723-9.
4. DeFelipe, J. (2011). The evolution of the brain, the human nature of cortical circuits, and intellectual creativity. Front. Neuroanat. *5*, *29*. https://doi.org/10.3389/fnana.2011.00029.
5. Herculano-Houzel, S., Mota, B., and Lent, R. (2006). Cellular scaling rules for rodent brains. Proc. Natl. Acad. Sci. USA *103*, 12138–12143. https://doi.org/10.1073/pnas.0604911103.
6. Herculano-Houzel, S. (2009). The human brain in numbers: a linearly scaled-up primate brain. Front. Hum. Neurosci. *3*, 31. https://doi.org/10.3389/neuro.09.031.2009.
7. Lancaster, M.A., Renner, M., Martin, C.-A., Wenzel, D., Bicknell, L.S., Hurles, M.E., Homfray, T., Penninger, J.M., Jackson, A.P., and Knoblich, J.A. (2013). Cerebral organoids model human brain development and microcephaly. Nature *501*, 373–379. https://doi.org/10.1038/nature12517.
8. Paşca, A.M., Sloan, S.A., Clarke, L.E., Tian, Y., Makinson, C.D., Huber, N., Kim, C.H., Park, J.-Y., O'Rourke, N.A., Nguyen, K.D., et al. (2015). Functional cortical neurons and astrocytes from human pluripotent stem cells in 3D culture. Nat. Methods *12*, 671–678. https://doi.org/10.1038/nmeth.3415.
9. Chiaradia, I., and Lancaster, M.A. (2020). Brain organoids for the study of human neurobiology at the interface of in vitro and in vivo. Nat. Neurosci. *23*, 1496–1508. https://doi.org/10.1038/s41593-020-00730-3.
10. Kyrousi, C., and Cappello, S. (2020). Using brain organoids to study human neurodevelopment, evolution and disease. Wiley Interdiscip. Rev. Dev. Biol. *9*, e347. https://doi.org/10.1002/wdev.347.
11. Cheroni, C., Trattaro, S., Caporale, N., López-Tobón, A., Tenderini, E., Sebastiani, S., Troglio, F., Gabriele, M., Bressan, R.B., Pollard, S.M., et al. (2022). Benchmarking brain organoid recapitulation of fetal corticogenesis. Transl. Psychiatry *12*, 520. https://doi.org/10.1038/s41398-022-02279-0.
12. Trujillo, C.A., Gao, R., Negraes, P.D., Gu, J., Buchanan, J., Preissl, S., Wang, A., Wu, W., Haddad, G.G., Chaim, I.A., et al. (2019). Complex Oscillatory Waves Emerging from Cortical Organoids Model Early Human Brain Network Development. Cell Stem Cell *25*, 558–569.e7. https://doi.org/10.1016/j.stem.2019.08.002.
13. Inak, G., Rybak-Wolf, A., Lisowski, P., Pentimalli, T.M., Jüttner, R., Glažar, P., Uppal, K., Bottani, E., Brunetti, D., Secker, C., et al. (2021). Defective metabolic programming impairs early neuronal morphogenesis in neural cultures and an organoid model of Leigh syndrome. Nat. Commun. *12*, 1929. https://doi.org/10.1038/s41467-021-22117-z.
14. Paşca, A.M., Park, J.-Y., Shin, H.-W., Qi, Q., Revah, O., Krasnoff, R., O'Hara, R., Willsey, A.J., Palmer, T.D., and Paşca, S.P. (2019). Human 3D cellular model of hypoxic brain injury of prematurity. Nat. Med. *25*, 784–791. https://doi.org/10.1038/s41591-019-0436-0.
15. Quadrato, G., Nguyen, T., Macosko, E.Z., Sherwood, J.L., Min Yang, S., Berger, D.R., Maria, N., Scholvin, J., Goldman, M., Kinney, J.P., et al. (2017). Cell diversity and network dynamics in photosensitive human brain organoids. Nature *545*, 48–53. https://doi.org/10.1038/nature22047.
16. Lancaster, M.A., and Knoblich, J.A. (2014). Generation of cerebral organoids from human pluripotent stem cells. Nat. Protoc. *9*, 2329–2340. https://doi.org/10.1038/nprot.2014.158.
17. Bhaduri, A., Andrews, M.G., Mancia Leon, W., Jung, D., Shin, D., Allen, D., Jung, D., Schmunk, G., Haeussler, M., Salma, J., et al. (2020). Cell stress in cortical organoids impairs molecular subtype specification. Nature *578*, 142–148. https://doi.org/10.1038/s41586-020-1962-0.
18. Giandomenico, S.L., Mierau, S.B., Gibbons, G.M., Wenger, L.M.D., Masullo, L., Sit, T., Sutcliffe, M., Boulanger, J., Tripodi, M., Derivery, E., et al. (2019). Cerebral organoids at the air–liquid interface generate diverse nerve tracts with functional output. Nat. Neurosci. *22*, 669–679. https://doi.org/10.1038/s41593-019-0350-2.
19. Giandomenico, S.L., Sutcliffe, M., and Lancaster, M.A. (2021). Generation and long-term culture of advanced cerebral organoids for studying later stages of neural development. Nat. Protoc. *16*, 579–602. https://doi.org/10.1038/s41596-020-00433-w.
20. Qian, X., Su, Y., Adam, C.D., Deutschmann, A.U., Pather, S.R., Goldberg, E.M., Su, K., Li, S., Lu, L., Jacob, F., et al. (2020). Sliced Human Cortical Organoids for Modeling Distinct Cortical Layer Formation. Cell Stem Cell *26*, 766–781.e9. https://doi.org/10.1016/j.stem.2020.02.002.
21. Szebényi, K., Wenger, L.M.D., Sun, Y., Dunn, A.W.E., Limegrover, C.A., Gibbons, G.M., Conci, E., Paulsen, O., Mierau, S.B., Balmus, G., and Lakatos, A. (2021). Human ALS/FTD brain organoid slice cultures display distinct early astrocyte and targetable neuronal pathology. Nat. Neurosci. *24*, 1542–1554. https://doi.org/10.1038/s41593-021-00923-4.
22. Tang, J., Zheng, H., Feng, Y., Zeng, J., and Ma, S. (2023). Attachment culture of cortical organoids at the microwell air-liquid interface. STAR Protoc. *4*, 102502. https://doi.org/10.1016/j.xpro.2023.102502.
23. Sharf, T., van der Molen, T., Glasauer, S.M.K., Guzman, E., Buccino, A.P., Luna, G., Cheng, Z., Audouard, M., Ranasinghe, K.G., Kudo, K., et al. (2022). Functional neuronal circuitry and oscillatory dynamics in human brain organoids. Nat. Commun. *13*, 4403. https://doi.org/10.1038/s41467-022-32115-4.
24. Wenzel, T.J., Le, J., He, J., Alcorn, J., and Mousseau, D.D. (2023). Fundamental Neurochemistry Review: Incorporating a greater diversity of cell types, including microglia, in brain organoid cultures improves clinical translation. J. Neurochem. *164*, 560–582. https://doi.org/10.1111/jnc.15741.
25. Le, S., Petersilie, L., Inak, G., Menacho-Pando, C., Kafitz, K.W., Rybak-Wolf, A., Rajewsky, N., Rose, C.R., and Prigione, A. (2021). Generation of human brain organoids for mitochondrial disease modeling. J. Vis. Exp. e62756. https://doi.org/10.3791/62756.
26. Velasco, S., Kedaigle, A.J., Simmons, S.K., Nash, A., Rocha, M., Quadrato, G., Paulsen, B., Nguyen, L., Adiconis, X., Regev, A., et al. (2019). Individual brain organoids reproducibly form cell diversity of the human cerebral cortex. Nature *570*, 523–527. https://doi.org/10.1038/s41586-019-1289-x.
27. Miura, Y., Li, M.-Y., Revah, O., Yoon, S.-J., Narazaki, G., and Paşca, S.P. (2022). Engineering brain assembloids to interrogate human neural circuits. Nat. Protoc. *17*, 15–35. https://doi.org/10.1038/s41596-021-00632-z.
28. Stoppini, L., Buchs, P.-A., and Muller, D. (1991). A simple method for organotypic cultures of nervous tissue. J. Neurosci. Methods *37*, 173–182. https://doi.org/10.1016/0165-0270(91)90128-m.
29. Lerchundi, R., Kafitz, K.W., Winkler, U., Färfers, M., Hirrlinger, J., and Rose, C.R. (2019). FRET-based imaging of intracellular ATP in organotypic brain slices. J. Neurosci. Res. *97*, 933–945. https://doi.org/10.1002/jnr.24361.
30. Mariani, J., Coppola, G., Zhang, P., Abyzov, A., Provini, L., Tomasini, L., Amenduni, M., Szekely, A., Palejev, D., Wilson, M., et al. (2015). FOXG1-Dependent Dysregulation of GABA/Glutamate Neuron Differentiation in Autism Spectrum Disorders. Cell *162*, 375–390. https://doi.org/10.1016/j.cell.2015.06.034.
31. Verkerke, M., Berdenis van Berlekom, A., Donega, V., Vonk, D., Sluijs, J.A., Butt, N.F., Kistemaker, L., de Witte, L.D., Pasterkamp, R.J., Middeldorp, J., and Hol, E.M. (2024). Transcriptomic and morphological

maturation of human astrocytes in cerebral organoids. Glia *72*, 362–374. https://doi.org/10.1002/glia.24479.
32. Atale, N., Gupta, S., Yadav, U.C.S., and Rani, V. (2014). Cell-death assessment by fluorescent and nonfluorescent cytosolic and nuclear staining techniques. J. Microsc. *255*, 7–19. https://doi.org/10.1111/jmi.12133.
33. De Paola, M., Pischiutta, F., Comolli, D., Mariani, A., Kelk, J., Lisi, I., Cerovic, M., Fumagalli, S., Forloni, G., and Zanier, E.R. (2023). Neural cortical organoids from self-assembling human iPSC as a model to investigate neurotoxicity in brain ischemia. J. Cerebr. Blood Flow Metabol. *43*, 680–693. https://doi.org/10.1177/0271678X231152023.
34. Karus, C., Ziemens, D., and Rose, C.R. (2015). Lactate rescues neuronal sodium homeostasis during impaired energy metabolism. Channels *9*, 200–208. https://doi.org/10.1080/19336950.2015.1050163.
35. Moskowitz, M.A., Lo, E.H., and Iadecola, C. (2010). The science of stroke: mechanisms in search of treatments. Neuron *67*, 181–198. https://doi.org/10.1152/jn.1987.57.3.869.
36. Daniele, S.G., Trummer, G., Hossmann, K.A., Vrselja, Z., Benk, C., Gobeske, K.T., Damjanovic, D., Andrijevic, D., Pooth, J.-S., Dellal, D., et al. (2021). Brain vulnerability and viability after ischaemia. Nat. Rev. Neurosci. *22*, 553–572. https://doi.org/10.1038/s41583-021-00488-y.
37. Cunnane, S.C., Trushina, E., Morland, C., Prigione, A., Casadesus, G., Andrews, Z.B., Beal, M.F., Bergersen, L.H., Brinton, R.D., de la Monte, S., et al. (2020). Brain energy rescue: an emerging therapeutic concept for neurodegenerative disorders of ageing. Nat. Rev. Drug Discov. *19*, 609–633. https://doi.org/10.1038/s41573-020-0072-x.
38. Iwata, R., Casimir, P., Erkol, E., Boubakar, L., Planque, M., Gallego López, I.M., Ditkowska, M., Gaspariunaite, V., Beckers, S., Remans, D., et al. (2023). Mitochondria metabolism sets the species-specific tempo of neuronal development. Science *379*, eabn4705. https://doi.org/10.1126/science.abn4705.
39. Lange, C., Turrero Garcia, M., Decimo, I., Bifari, F., Eelen, G., Quaegebeur, A., Boon, R., Zhao, H., Boeckx, B., Chang, J., et al. (2016). Relief of hypoxia by angiogenesis promotes neural stem cell differentiation by targeting glycolysis. EMBO J. *35*, 924–941. https://doi.org/10.15252/embj.201592372.
40. Mansour, A.A., Gonçalves, J.T., Bloyd, C.W., Li, H., Fernandes, S., Quang, D., Johnston, S., Parylak, S.L., Jin, X., and Gage, F.H. (2018). An in vivo model of functional and vascularized human brain organoids. Nat. Biotechnol. *36*, 432–441. https://doi.org/10.1038/nbt.4127.
41. Cakir, B., Xiang, Y., Tanaka, Y., Kural, M.H., Parent, M., Kang, Y.-J., Chapeton, K., Patterson, B., Yuan, Y., He, C.-S., et al. (2019). Engineering of human brain organoids with a functional vascular-like system. Nat. Methods *16*, 1169–1175. https://doi.org/10.1038/s41592-019-0586-5.
42. Crouch, E.E., Bhaduri, A., Andrews, M.G., Cebrian-Silla, A., Diafos, L.N., Birrueta, J.O., Wedderburn-Pugh, K., Valenzuela, E.J., Bennett, N.K., Eze, U.C., et al. (2022). Ensembles of endothelial and mural cells promote angiogenesis in prenatal human brain. Cell *185*, 3753–3769.e18. https://doi.org/10.1016/j.cell.2022.09.004.
43. Del Dosso, A., Urenda, J.-P., Nguyen, T., and Quadrato, G. (2020). Upgrading the physiological relevance of human brain organoids. Neuron *107*, 1014–1028. https://doi.org/10.1016/j.neuron.2020.08.029.
44. Samarasinghe, R.A., Miranda, O.A., Buth, J.E., Mitchell, S., Ferando, I., Watanabe, M., Allison, T.F., Kurdian, A., Fotion, N.N., Gandal, M.J., et al. (2021). Identification of neural oscillations and epileptiform changes in human brain organoids. Nat. Neurosci. *24*, 1488–1500. https://doi.org/10.1038/s41593-021-00906-5.
45. Beghin, A., Grenci, G., Sahni, G., Guo, S., Rajendiran, H., Delaire, T., Mohamad Raffi, S.B., Blanc, D., de Mets, R., Ong, H.T., et al. (2022). Automated high-speed 3D imaging of organoid cultures with multi-scale phenotypic quantification. Nat. Methods *19*, 881–892. https://doi.org/10.1038/s41592-022-01508-0.
46. Yildirim, M., Delepine, C., Feldman, D., Pham, V.A., Chou, S., Ip, J., Nott, A., Tsai, L.-H., Ming, G.-L., So, P.T.C., and Sur, M. (2022). Label-free three-photon imaging of intact human cerebral organoids for tracking early events in brain development and deficits in Rett syndrome. Elife *11*, e78079. https://doi.org/10.7554/eLife.78079.
47. Mayhew, C.N., and Singhania, R. (2023). A review of protocols for brain organoids and applications for disease modeling. STAR Protoc. *4*, 101860. https://doi.org/10.1016/j.xpro.2022.101860.
48. Miura, Y., Li, M.-Y., Birey, F., Ikeda, K., Revah, O., Thete, M.V., Park, J.-Y., Puno, A., Lee, S.H., Porteus, M.H., and Pașca, S.P. (2020). Generation of human striatal organoids and cortico-striatal assembloids from human pluripotent stem cells. Nat. Biotechnol. *38*, 1421–1430. https://doi.org/10.1038/s41587-020-00763-w.
49. Kim, H., Xu, R., Padmashri, R., Dunaevsky, A., Liu, Y., Dreyfus, C.F., and Jiang, P. (2019). Pluripotent stem cell-derived cerebral organoids reveal human oligodendrogenesis with dorsal and ventral origins. Stem Cell Rep. *12*, 890–905. https://doi.org/10.1016/j.stemcr.2019.04.011.
50. Marton, R.M., Miura, Y., Sloan, S.A., Li, Q., Revah, O., Levy, R.J., Huguenard, J.R., and Pașca, S.P. (2019). Differentiation and maturation of oligodendrocytes in human three-dimensional neural cultures. Nat. Neurosci. *22*, 484–491. https://doi.org/10.1038/s41593-018-0316-9.
51. Madhavan, M., Nevin, Z.S., Shick, H.E., Garrison, E., Clarkson-Paredes, C., Karl, M., Clayton, B.L.L., Factor, D.C., Allan, K.C., Barbar, L., et al. (2018). Induction of myelinating oligodendrocytes in human cortical spheroids. Nat. Methods *15*, 700–706. https://doi.org/10.1038/s41592-018-0081-4.
52. Al-mhanawi, B., Marti, M.B., Morrison, S.D., Gupta, P., Alani, M., Noakes, P.G., Wolvetang, E.J., and Shaker, M.R. (2023). Protocol for generating embedding-free brain organoids enriched with oligodendrocytes. STAR Protoc. *4*, 102725. https://doi.org/10.1016/j.xpro.2023.102725.
53. Fair, S.R., Julian, D., Hartlaub, A.M., Pusuluri, S.T., Malik, G., Summerfied, T.L., Zhao, G., Hester, A.B., Ackerman, W.E., Hollingsworth, E.W., et al. (2020). Electrophysiological Maturation of Cerebral Organoids Correlates with Dynamic Morphological and Cellular Development. Stem Cell Rep. *15*, 855–868. https://doi.org/10.1016/j.stemcr.2020.08.017.
54. Negraes, P.D., Trujillo, C.A., Yu, N.-K., Wu, W., Yao, H., Liang, N., Lautz, J.D., Kwok, E., McClatchy, D., Diedrich, J., et al. (2021). Altered network and rescue of human neurons derived from individuals with early-onset genetic epilepsy. Mol. Psychiatr. *26*, 7047–7068. https://doi.org/10.1038/s41380-021-01104-2.
55. Sakaguchi, H., Ozaki, Y., Ashida, T., Matsubara, T., Oishi, N., Kihara, S., and Takahashi, J. (2019). Self-organized synchronous calcium transients in a cultured human neural network derived from cerebral organoids. Stem Cell Rep. *13*, 458–473. https://doi.org/10.1016/j.stemcr.2019.05.029.
56. Gordon, A., Yoon, S.-J., Tran, S.S., Makinson, C.D., Park, J.Y., Andersen, J., Valencia, A.M., Horvath, S., Xiao, X., Huguenard, J.R., et al. (2021). Long-term maturation of human cortical organoids matches key early postnatal transitions. Nat. Neurosci. *24*, 331–342. https://doi.org/10.1038/s41593-021-00802-y.
57. Birey, F., Andersen, J., Makinson, C.D., Islam, S., Wei, W., Huber, N., Fan, H.C., Metzler, K.R.C., Panagiotakos, G., Thom, N., et al. (2017). Assembly of functionally integrated human forebrain spheroids. Nature *545*, 54–59. https://doi.org/10.1038/nature22330.
58. Zourray, C., Kurian, M.A., Barral, S., and Lignani, G. (2022). Electrophysiological Properties of Human Cortical Organoids: Current State of the Art and Future Directions. Front. Mol. Neurosci. *15*, 839366. https://doi.org/10.3389/fnmol.2022.839366.
59. Fellin, T., Gomez-Gonzalo, M., Gobbo, S., Carmignoto, G., and Haydon, P.G. (2006). Astrocytic glutamate is not necessary for the generation of epileptiform neuronal activity in hippocampal slices. J. Neurosci. *26*, 9312–9322. https://doi.org/10.1523/JNEUROSCI.2836-06.2006.
60. Rouach, N., Koulakoff, A., Abudara, V., Willecke, K., and Giaume, C. (2008). Astroglial metabolic networks sustain hippocampal synaptic transmission. Science *322*, 1551–1555. https://doi.org/10.1126/science.1164022.
61. Karus, C., Mondragão, M.A., Ziemens, D., and Rose, C.R. (2015). Astrocytes restrict discharge duration and neuronal sodium loads during recurrent network activity. Glia *63*, 936–957. https://doi.org/10.1002/glia.22793.
62. Mody, I., Lambert, J.D., and Heinemann, U. (1987). Low extracellular magnesium induces epileptiform activity and spreading depression in rat hippocampal slices. J. Neurophysiol. *57*, 869–888. https://doi.org/10.1152/jn.1987.57.3.869.
63. Garaschuk, O., Linn, J., Eilers, J., and Konnerth, A. (2000). Large-scale oscillatory calcium waves in the immature cortex. Nat. Neurosci. *3*, 452–459. https://doi.org/10.1038/74823.
64. Renner, H., Grabos, M., Becker, K.J., Kagermeier, T.E., Wu, J., Otto, M., Peischard, S., Zeuschner, D., TsyTsyura, Y., Disse, P., et al. (2020). A fully automated high-throughput workflow for 3D-based chemical screening in human midbrain organoids. Elife *9*, e52904. https://doi.org/10.7554/eLife.52904.
65. Paulsen, B., Velasco, S., Kedaigle, A.J., Pigoni, M., Quadrato, G., Deo, A.J., Adiconis, X., Uzquiano, A., Sartore, R., Yang, S.M., et al. (2022). Autism genes converge on asynchronous development of shared neuron classes. Nature *602*, 268–273. https://doi.org/10.1038/s41586-021-04358-6.

66. Garaschuk, O., Hanse, E., and Konnerth, A. (1998). Developmental profile and synaptic origin of early network oscillations in the CA1 region of rat neonatal hippocampus. J. Physiol. *507*, 219–236. https://doi.org/10.1111/j.1469-7793.1998.219bu.x.
67. Hanganu-Opatz, I.L. (2010). Between molecules and experience: role of early patterns of coordinated activity for the development of cortical maps and sensory abilities. Brain Res. Rev. *64*, 160–176. https://doi.org/10.1016/j.brainresrev.2010.03.005.
68. Gaston-Breton, R., Maïza Letrou, A., Hamoudi, R., Stonestreet, B.S., and Mabondzo, A. (2023). Brain organoids for hypoxic-ischemic studies: from bench to bedside. Cell. Mol. Life Sci. *80*, 318. https://doi.org/10.1007/s00018-023-04951-0.
69. Khacho, M., Clark, A., Svoboda, D.S., Azzi, J., MacLaurin, J.G., Meghaizel, C., Sesaki, H., Lagace, D.C., Germain, M., Harper, M.-E., et al. (2016). Mitochondrial Dynamics Impacts Stem Cell Identity and Fate Decisions by Regulating a Nuclear Transcriptional Program. Cell Stem Cell *19*, 232–247. https://doi.org/10.1016/j.stem.2016.04.015.
70. Brunetti, D., Dykstra, W., Le, S., Zink, A., and Prigione, A. (2021). Mitochondria in Neurogenesis: Implications for Mitochondrial Diseases. Stem Cell. *39*, 1289–1297. https://doi.org/10.1002/stem.3425.
71. Wang, S.-n., Wang, Z., Wang, X.-y., Zhang, X.-p., Xu, T.-y., and Miao, C.-y. (2023). Humanized cerebral organoids-based ischemic stroke model for discovering of potential anti-stroke agents. Acta Pharmacol. Sin. *44*, 513–523. https://doi.org/10.1038/s41401-022-00986-4.
72. Lerchundi, R., Huang, N., and Rose, C.R. (2020). Quantitative imaging of changes in astrocytic and neuronal adenosine triphosphate using two different variants of ATeam. Front. Cell. Neurosci. *14*, 80. https://doi.org/10.3389/fncel.2020.00080.
73. Pape, N., and Rose, C.R. (2023). Activation of TRPV4 channels promotes the loss of cellular ATP in organotypic slices of the mouse neocortex exposed to chemical ischemia. J. Physiol. *601*, 2975–2990. https://doi.org/10.1113/JP284430.
74. Kelley, K.W., and Paşca, S.P. (2022). Human brain organogenesis: Toward a cellular understanding of development and disease. Cell *185*, 42–61. https://doi.org/10.1016/j.cell.2021.10.003.
75. Ye, B. (2023). Approaches to vascularizing human brain organoids. PLoS Biol. *21*, e3002141. https://doi.org/10.1371/journal.pbio.3002141.
76. Park, D.S., Kozaki, T., Tiwari, S.K., Moreira, M., Khalilnezhad, A., Torta, F., Olivié, N., Thiam, C.H., Liani, O., Silvin, A., et al. (2023). iPS-cell-derived microglia promote brain organoid maturation via cholesterol transfer. Nature *623*, 397–405. https://doi.org/10.1038/s41586-023-06713-1.
77. Schafer, S.T., Mansour, A.A., Schlachetzki, J.C.M., Pena, M., Ghassemzadeh, S., Mitchell, L., Mar, A., Quang, D., Stumpf, S., Ortiz, I.S., et al. (2023). An in vivo neuroimmune organoid model to study human microglia phenotypes. Cell *186*, 2111–2126.e20. https://doi.org/10.1016/j.cell.2023.04.022.
78. Wang, X., Sterr, M., Burtscher, I., Chen, S., Hieronimus, A., Machicao, F., Staiger, H., Häring, H.U., Lederer, G., Meitinger, T., et al. (2018). Genome-wide analysis of PDX1 target genes in human pancreatic progenitors. Mol. Metabol. *9*, 57–68. https://doi.org/10.1016/j.molmet.2018.01.011.
79. Lorenz, C., Lesimple, P., Bukowiecki, R., Zink, A., Inak, G., Mlody, B., Singh, M., Semtner, M., Mah, N., Auré, K., et al. (2017). Human iPSC-Derived Neural Progenitors Are an Effective Drug Discovery Model for Neurological mtDNA Disorders. Cell Stem Cell *20*, 659–674.e9. https://doi.org/10.1016/j.stem.2016.12.013.
80. Lee, J.-H., Park, I.-H., Gao, Y., Li, J.B., Li, Z., Daley, G.Q., Zhang, K., and Church, G.M. (2009). A robust approach to identifying tissue-specific gene expression regulatory variants using personalized human induced pluripotent stem cells. PLoS Genet. *5*, e1000718. https://doi.org/10.1371/journal.pgen.1000718.
81. Rifes, P., Isaksson, M., Rathore, G.S., Aldrin-Kirk, P., Møller, O.K., Barzaghi, G., Lee, J., Egerod, K.L., Rausch, D.M., Parmar, M., et al. (2020). Modeling neural tube development by differentiation of human embryonic stem cells in a microfluidic WNT gradient. Nat. Biotechnol. *38*, 1265–1273. https://doi.org/10.1038/s41587-020-0525-0.
82. Lerchundi, R., Kafitz, K.W., Färfers, M., Beyer, F., Huang, N., and Rose, C.R. (2019). Imaging of intracellular ATP in organotypic tissue slices of the mouse brain using the FRET-based sensor ATeam1. 03YEMK. J. Vis. Exp. e60294. https://doi.org/10.1002/jnr.24361.
83. Schindelin, J., Arganda-Carreras, I., Frise, E., Kaynig, V., Longair, M., Pietzsch, T., Preibisch, S., Rueden, C., Saalfeld, S., Schmid, B., et al. (2012). Fiji: an open-source platform for biological-image analysis. Nat. Methods *9*, 676–682. https://doi.org/10.1038/nmeth.2019.
84. Mishra, P., Pandey, C.M., Singh, U., Gupta, A., Sahu, C., and Keshri, A. (2019). Descriptive statistics and normality tests for statistical data. Ann. Card Anaesth. *22*, 67–72. https://doi.org/10.4103/aca.aca_157_18.
85. Nayak, B.K., and Hazra, A. (2011). How to choose the right statistical test? Indian J. Ophthalmol. *59*, 85–86. https://doi.org/10.1152/jn.1987.57.3.869.

STAR★METHODS

KEY RESOURCES TABLE

REAGENT or RESOURCE	SOURCE	IDENTIFIER
Antibodies		
DAPI (4′,6-Diamidino-2-Phenylindole, Dilactate)	Thermo Fisher Scientific (Invitrogen™)	Cat# D3571, RRID:AB_2307445
Donkey anti-Guinea Pig IgG (H+L), highly crossabsorbed CF™ 488A	Sigma-Aldrich	Cat# SAB4600033, RRID:AB_2890881
Donkey anti-Mouse IgG Polyclonal antibody, Cyanine 3 Conjugated	Millipore	Cat# AP192C, RRID:AB_92642
Donkey anti-Rabbit IgG (H+L) Ready Probes Secondary Antibody, Alexa Fluor™ 488	Thermo Fisher Scientific (Invitrogen™)	Cat# R37118, RRID:AB_2556546
Donkey anti-Rabbit IgG Polyclonal antibody, Cyanine 3 Conjugated	Jackson Immuno Research	Cat# 711-165-152, RRID:AB_2307443
Goat anti-Guinea Pig IgG (H+L), highly crossadsorbed secondary antibody, Alexa Fluor™ 488	Thermo Fisher Scientific (Invitrogen™)	Cat# A-11076, RRID:AB_2534120
Goat anti-Guinea Pig IgG (H+L), highly crossadsorbed secondary antibody, Alexa Fluor™ 594	Thermo Fisher Scientific (Invitrogen™)	Cat# A-11076, RRID:AB_2534120
Goat anti-Rabbit IgG (H+L) Cross-Adsorbed Secondary Antibody, Alexa Fluor ™ 488	Thermo Fisher Scientific (Invitrogen™)	Cat# A-11008, RRID:AB_143165
Goat anti-Rabbit IgG (H+L) Cross-Adsorbed Secondary Antibody, Alexa Fluor ™ 594	Thermo Fisher Scientific (Invitrogen™)	Cat# A-11012, RRID:AB_2534079
Goat anti-Mouse IgG (H+L) Cross-Adsorbed Secondary Antibody, Alexa Fluor™ 488	Thermo Fisher Scientific (Invitrogen™)	Cat# A-11001, RRID:AB_2534069
Goat anti-Mouse IgG (H+L) Cross-Adsorbed Secondary Antibody, Alexa Fluor™ 594	Thermo Fisher Scientific (Invitrogen™)	Cat# A-11005, RRID:AB_2534073
Guinea Pig polyclonal anti-GFAP	Synaptic Systems	Cat# 173 004, RRID:AB_10641162
Guinea Pig polyclonal anti-MAP2	Synaptic Systems	Cat# 188 004, RRID:AB_2138181
Guinea Pig polyclonal anti-VGLUT1	Synaptic Systems	Cat# 135 304, RRID:AB_887878
Hoechst 33342	Thermo Fisher Scientific (Invitrogen™)	Cat# H3570
Mouse monoclonal anti-PSD95	Abcam	Cat# ab2723, RRID:AB_303248
Mouse monoclonal anti-PSD95, clone K28/43	Millipore	Cat# MABN68; RRID:AB_10807979
Mouse monoclonal anti-ß-Tubulin III	Sigma-Aldrich	Cat#T8578; RRID: AB_1841228
Rabbit monoclonal anti-S100ß	Abcam	Cat# ab52642, RRID:AB_882426
Rabbit polyclonal anti-CTIP2	Abcam	Cat# ab82701, RRID:AB_1860617
Rabbit polyclonal anti-GFAP	Dako	ZO334
Rabbit polyclonal anti-Homer1	Synaptic systems	Cat# 160 003, RRID:AB_887730

(*Continued on next page*)

Continued

REAGENT or RESOURCE	SOURCE	IDENTIFIER
Rabbit polyclonal anti-PAX6	BioLegend	Cat# 901301, RRID:AB_2565003
Rabbit polyclonal anti-Synapsin 1	Thermo Fisher Scientific (Invitrogen™)	Cat# A-6442, RRID:AB_2536207
Bacterial and virus strains		
ssAAV-2/2-hSyn1- ATeam1.03YEMK-WPREhGHp(A)	ETH Zürich	v244
Chemicals, peptides, and recombinant proteins		
(+)-Sodium L-ascorbate	Sigma-Aldrich	Cat#A4034; CAS: 134-03-2
16% Formaldehyde	Thermo Fisher Scientific (Thermo Scientific™)	Cat#28908
2-Deoxy-D-Glucose	Apollo Scientific	Cat#OR3900T; CAS: 154-17-6
2-Mercaptoethanol	Thermo Fisher Scientific (Gibco™)	Cat#31350010; CAS: 60-24-2
Adenosine 5′-triphosphate magnesium salt	Sigma-Aldrich	Cat#A9187; CAS: 74804-12-9
Alexa Fluor 488	Thermo Fisher Scientific (Invitrogen™)	Cat#A10436
Anti-Adherence Rinsing solution	Stemcell Technologies	Cat#7010
B-27 Supplement (50x)	Thermo Fisher Scientific (Gibco™)	Cat#17504044
B-27™ Supplement (50x) minus Vitamin A	Thermo Fisher Scientific (Gibco™)	Cat#12587001
Bicuculline methiodide	Sigma-Aldrich	Cat#14343; CAS: 40709-69-1
Calcium chloride	Fluka/Honeywell	CAS: 10035-04-8
Chemically Defined Lipid Concentrate	Thermo Fisher Scientific (Gibco™)	Cat#11905031
cis-4,7,10,13,16,19- Docosahexaenoic acid (DHA)	Sigma-Aldrich	Cat#D2534-25MG; CAS: 6217-54-5
Corning Matrigel Growth Factor Reduced (GFR) Basement membrane matrix, Phenol Red-free, LDEV-free	Corning	Cat#356231
D.E.R.® 736	Serva	Cat#18247.01
Dibutyryl cAMP	Stemcell Technologies	Cat#73886; CAS: 362-74-3
Dimethylaminomethanol	Serva	Cat#20130
DL-APV	HelloBio	Cat#HB0251; CAS: 76326-31-3
DMEM/F12, HEPES	Thermo Fisher Scientific (Gibco™)	Cat#31330038
Dimethylsulfoxide (DMSO)	Sigma-Aldrich	Cat#D8418; CAS: 6768-5
Donkey Serum	Sigma-Aldrich	Cat#S30
Dorsomorphin	Sigma	Cat# P5499-5MG; CAS: 866405-64-3
Dulbecco's Phosphate Buffered Saline	Thermo Fisher Scientific (Gibco™)	Cat#14287080
Dulbecco's Phosphate Buffered Saline, without calcium and magnesium	Thermo Fisher Scientific (Gibco™)	Cat#14190144
ERL-4221D, Epoxycyclohexylmethyl-3, 4epoxycyclohexylcarboxylate	Serva	Cat#21041.02
Fetal Bovine Serum	Thermo Fisher Scientific (Gibco™)	Cat#10270106; CAS: 9014-81-7
Fixogum	Marabu	Cat#29010017000
Geltrex™ hESC-Qualified, Ready-To-Use, Reduced Growth Factor Basement Membrane Matrix	Thermo Fisher Scientific (Gibco™)	Cat#A1569601
Glasgow-MEM	Thermo Fisher Scientific (Gibco™)	Cat#11710035
Glucose	Caelo	Cat#2580; CAS: 14431-43-7
Glutamax	Thermo Fisher Scientific (Gibco™)	Cat#35050061
Glutaraldehyde 25%	Serva	Cat#23114
Goat Serum	Thermo Fisher Scientific (Gibco™)	Cat#16210064

(*Continued on next page*)

Continued

REAGENT or RESOURCE	SOURCE	IDENTIFIER
Guanosine 5′-triphosphate sodium salt hydrate	Sigma-Aldrich	Cat#G8877; CAS: 36051-31-7
Hank's Balanced Salt Solution	Sigma-Aldrich	Cat#H9394
Heparin	Sigma-Aldrich	Cat#H3149-25KU; CAS: 9045-22-1
HEPES	Roth	Cat#HN78.2; CAS:7365-45-9
Human BDNF	MACS Miltenyi	Cat#130-096-286; CAS: 218441-99-7
Knockout Serum Replacement (KSR)	Thermo Fisher Scientific (Gibco™)	Cat#10828010
KnockOut™ (KO) DMEM	Thermo Fisher Scientific (Gibco™)	Cat#10829-018
LB Agar (Lennox L Agar)	Sigma-Aldrich	Cat#L2897
L-Glutamic acid monosodium salt hydrate	Sigma-Aldrich	Cat#G1626; CAS: 142-47-2
L-Glutamine	Thermo Fisher Scientific (Gibco™)	Cat#25030081; CAS: 56-85-9
Low Melting Point Agarose	Thermo Fisher Scientific (Gibco™)	Cat#55174B; CAS: 9012-36-6
Magnesium chloride	Carl Roth	Cat#2189.1; CAS: 7791-18-6
MEM Non-Essential Amino Acid Solution	Thermo Fisher Scientific (Gibco™)	Cat#11140-050
MOWIOL® 4–88 Reagent	Millipore	Cat#475904-M; CAS: 9002-89-5
MycoZap Plus-CL	Lonza	Cat#VZA-2012
N-2 Supplement (100x)	Thermo Fisher Scientific (Gibco™)	Cat#17502048; CAS: 10102-18-8
NBQX disodium salt	BioTrend	Cat#NB-48-0652
Neurobasal-A Medium	Thermo Fisher Scientific (Gibco™)	108880-22
Nonenylsuccinic Anhydride Pure	Serva	Cat#30812.01
Oregon Green 488 BAPTA-1 AM, cell permeant	Thermo Fisher Scientific (Invitrogen™)	Cat#O6807; CAS: 244167-57-5
Osmium tetroxide	Science Services	Cat#E19110
Paraformaldehyde	Sigma-Aldrich	Cat#158127; CAS: 30525-89-4
Penicilin-Streptomycin (10.000 U/ml)	Thermo Fisher Scientific (Gibco™)	Cat#15140122
Phosphotungstic acid hydrate	Merck Supelco	Cat#1005820100
Pluronic F-127	Thermo Fisher Scientific (Invitrogen™)	Cat#P6867
Potassium chloride	Carl Roth	Cat#6781.1; CAS: 7447-40-7
Potassium methanesulfonate	Sigma-Aldrich	Cat#83000; CAS: 2386-56-3
ProLong Glass Antifade Mountant	Thermo Fisher Scientific (Invitrogen™)	Cat#P36980
Propidium iodide (solution)	Thermo Fisher Scientific (Invitrogen™)	Cat#P3566
Recombinant Human EGF Protein, CF	R & D Systems	Cat#236-EG-200; CAS: 62253-63-8
Recombinant Human FGF basic/FGF2/bFGF (145 aa) Protein, CF	R & D Systems	Cat#3718-FB-100; CAS: 106096-93-9
Recombinant Human NT-3	Peprotech	Cat# PPT-450-03-50; CAS: 130939-66-1
RNase A, DNase and Protease-free	Thermo Scientific ™	Cat#EN0531
ROCK inhibitor, Y-237632, dihydrochloride	Enzo Life Sciences	Cat#ALX-270-333M005; CAS: 12983038-2
SB431542	Cayman Chemical Company	Cat#13031; CAS: 301836-41-9
Sodium azide	Honeywell	Cat#13412H; CAS: 26628-22-8
Sodium bicarbonate	Sigma-Aldrich	Cat#S6014; CAS: 14455-8
Sodium cacodylate	Serva	Cat#15540
Sodium chloride	Carl Roth	Cat#3957; CAS: 764714-5
Sodium di-Hydrogen Phosphate 1-hydrate	AppliChem	Cat#131965; CAS: 10049-21-5
Sodium pyruvate	Thermo Fisher Scientific (Gibco™)	Cat#11360070; CAS: 113-24-6
SSC-Puffer (20 X)	Thermo Scientific Chemicals	Cat#J60839.K2
StemMACS ™ iPS Brew XF	Miltenyi Biotec	Cat#130-107-086
StemMACS ™ iPS Brew XF 50x Supplements	Miltenyi Biotec	Cat#130-107-087

(*Continued on next page*)

Continued

REAGENT or RESOURCE	SOURCE	IDENTIFIER
StemPro™ Accutase™ Cell Dissociation Reagent	Thermo Fisher Scientific (Gibco™)	Cat#A1110501
Super Glue Gel	UHU	Cat#63261
Tetrodotoxin citrate	Biozol/ HelloBio	Cat#HLN-HB1035; CAS18660-81-6
Triton ™ X-100	Sigma-Aldrich	Cat#X100; CAS: 903619-5
Triton X-100	AppliChem	Cat#A4975,0500; CAS: 9002-93-1
Trypan Blue Solution	Sigma-Aldrich	Cat#T8154; CAS: 7257-1
Tween® 20	Sigma-Aldrich	Cat#P1379; CAS: 9005-64-5
Uranyl Acetate	Merck	Cat#8473
Wnt Antagonist I (IWR1)	EMD Millipore Corp	Cat#3378738; CAS: 1127442-82-3
γ-Aminobutyric acid (GABA)	Sigma-Aldrich	Cat#P28352; CAS: 5612-2
Critical commercial assays		
N/A	N/A	N/A
Deposited data		
Raw and analyzed data	This paper	https://researchdata.hhu.de/handle/123456789/152
Figure 1	This paper	https://doi.org/10.25838/d5p-56
Figure 2	This paper	https://doi.org/10.25838/d5p-57
Figure 3	This paper	https://doi.org/10.25838/d5p-59
Figure 4	This paper	https://doi.org/10.25838/d5p-62
Figure 5	This paper	https://doi.org/10.25838/d5p-58
Figure 6	This paper	https://doi.org/10.25838/d5p-61
Figure 7	This paper	https://doi.org/10.25838/d5p-60
Figure S1	This paper	https://doi.org/10.25838/d5p-63
Experimental models: Cell lines		
Human: HMGUi001-A (XM001) iPSC	Helmhotz Zentrum München (HMGU)	RRID:CVCL_WJ49, https://hpscreg.eu/cellline/HMGUi001-A; Wang et al.[78]
Human: HHUUKDi009-A (TFBJ) iPSC	Heinrich Heine University Düsseldorf (HHUUKD)	RRID:CVCL_B3T9, https://hpscreg.eu/cellline/HHUUKDi009-A; Lorenz et al.[79]
Human: HVRDi004-B (PGP1) iPSC	Harvard University (HVRD)	RRID:CVCL_F182; https://hpscreg.eu/cell-line/HVRDi004-B; Lee et al.[80]
Software and algorithms		
Adobe Photoshop CS6	Adobe Inc.	RRID:SCR_014199
Affinity Designer	Serif (Europe) Ltd	RRID:SCR_016952
Excel 2016 / 2021	Microsoft Office Professional Plus 2016 / 2021	N/A
EZ- C1 Silver Version 3.91	Nikon	N/A
FluoView300	Olympus Deutschland GmbH	N/A
FluoView5.0	Olympus Europe	N/A
ImageJ	Schneider et al. (2012)	https://imagej.nih.gov/ij/; RRID:SCR_003070
NIS-Elements 3.2/ 4.5/ 5.00 Advanced Research	Nikon	RRID:SCR_014329
Origin Pro 2020 / Orgin Pro 2021	Origin Lab corporation	RRID:SCR_014212
Patch Master v2x53	HEKA Elektronik	N/A

(*Continued on next page*)

Continued

REAGENT or RESOURCE	SOURCE	IDENTIFIER
Other		
6-well plates	TPP	Cat#92006
6-well plates	Sarstedt	Cat#83.3920
96-well plate, BIOFLOAT	faCellitate GmbH	Cat#F202003
96-well, Ultra Low Cluster, U-Bottom, Ultra Low Attachment	Corning	Cat#7007
Adhesion slides, SuperFrost Plus	VWR	Cat#631-0108
AggreWell™ 800	Stemcell Technologies	Cat#34815
CO_2 Incubator, CB170	Binder	Cat#9040-0163
CO_2 Incubator, Heracell 240i	Thermo Fisher Scientific	Cat#51032875
Cover glasses	VWR	Cat#631-0135
Filter tips (10/ 20 µl), sterile	Starlab	Cat#S1120-3810
Filter tips (100, 1000 µl), sterile	Biozym	Cat#VT0230, Cat#VT0270
Greiner centrifuge tubes (15 ml)	Sigma-Aldrich	Cat#T1818
Improved Neubauer Counting Chamber	VWR	Cat#631-0696
Injekt Solo 1 ml/ Luer	Braun	Cat#4010-200V0
Injekt Solo 10 ml/ Luer	Braun	Cat#4606108V
Millicell Cell Culture Inserts	Millipore	Cat#PICM0RG50
Needle for single usage (23G x 1″ TW)	Neoject	Cat#10016
Needle Puller, PP-830	Narishige	N/A
Orbital Shaker, Unimax 1010	Heidolph	543-12310-00
Pasteur pipettes, glass	Brand	Cat#747715
Pasteur pipettes, plastic 3 ml	Heinz Herenz	Cat#1131303
Petri dish (35 mm)	Sarstedt	Cat#83.3900
Polystyrene Petri dish (100 mm)	Greiner Bio-One	Cat#664161
Power Supply Unit, NGB	Rohde & Schwarz	N/A
Power Supply Unit, DF-1730SB-3A	McVoice	N/A
Pressure Application System, PDES-01DXH-LA4-S	Npi electronics	N/A
Qualitative filter paper	VWR	Cat#516-0813
SafeSeal tube, 1.5 ml	Sarstedt	Cat#72.706
Serological pipettes (5, 10, 25 ml)	Greiner Bio-One	Cat#606-180, Cat#612-3700, 612-Cat#3698
Super glue gel	UHU	Cat#63261
Surface protector, Benchkote	Whatman	Cat#WHA2300916
Thermoblock, TB2	Biometra	Discontinued
Tissue culture hood, HeraSafe	Thermo Fisher Scientific	Cat#51022515
Tissue culture hood, Maxisafe 2030i	Thermo Fisher Scientific	Cat#51032711
Vibratome, Microm HM 650 V	Thermo Fisher Scientific	Discontinued
Wilkinson Classic Razor Blade	Wilkinson Sword	Cat#70517470

RESOURCE AVAILABILITY

Lead contact

Further information and requests for resources and reagents should be directed to and will be fulfilled by the lead contact, Christine R. Rose (rose@hhu.de).

Materials availability

This study did not generate new unique reagents, chemicals or materials.

Data and code availability

- All data reported in this paper will be shared by the lead contact upon request.
- This paper does not report original code.
- Any additional information required to reanalyse the data reported in this paper is available from the lead contact upon request.

EXPERIMENTAL MODEL AND STUDY PARTICIPANT DETAILS

Cell lines

The human iPSC lines HMGUi001-A,[78] HHUUKDi009-A[79] and HVRDi004-B,[80] derived from healthy individuals, were used.

Human iPSC culture

Human induced pluripotent stem cells (iPSCs) were established before. We used both male and female iPSCs for cBOS generation from three healthy human iPSC lines to ensure a robust, donor-independent outcome. HMGUi001-A (XM001) iPSCs were derived from fibroblasts using episomal reprogramming from a healthy, 50 years old female.[78] HHUUKDi009-A (TFBJ) iPSCs were derived from foreskin fribroblasts using episomal reprogramming from a healthy male neonate.[79] HVRDi004-B (PGP1) iPSCs were derived from fibroblasts using plasmid reprogramming from a healthy, 55 years old male.[80] iPSCs were cultured under feeder-free conditions in 6-well plates (TPP) coated with Matrigel (Corning) or Geltrex (Thermo Fisher Scientific), which both mimic extracellular matrix. iPSCs were kept in iPS Brew medium (Miltenyi Biotec) at 37°C, 5% CO_2, 5% O_2, maintained by daily media changes and passaged at 70–80% confluency. 10 μM Rho-associated protein kinase (ROCK, Enzo Life Sciences) inhibitor was added to increase cell survival. All iPSC lines were routinely monitored to ensure that they are always negative for mycoplasma contamination. Ethical approval for using control human iPSCs in a pseudo-anonymized fashion was obtained from the Ethic Committee of the University Clinic Düsseldorf (study number 2019-681 approved on October 11, 2019).

METHOD DETAILS

Generation of cortical brain organoids from human iPSC culture

Cortical brain organoids were generated using protocols based on the aggregation of iPSCs in U-bottom 96-well plates as well as in AggreWell plates. The 96-well plate-based protocol was established and described by Le and colleagues,[25] and in an earlier version by Velasco and colleagues.[26] In brief, human iPSCs were washed once with Phosphate Buffered Saline (PBS) and detached from 6-well plates by incubation with 500 μl Accutase (Thermo Fisher Scientific) per well for 5 minutes at 37°C. Next, 1 ml of iPS Brew medium was added and cells were dissociated by carefully pipetting them up and down. The cell suspension was transferred to a 15 ml falcon tube and centrifuged at 125 rcf for 5 minutes at room temperature.

After aspirating the supernatant, the cell pellet was resuspended in 3 ml freshly prepared Cortical Differentiation Medium I (CDMI) at room temperature (Figure 1A). CDMI is based on Glasgow-MEM (Thermo Fisher Scientific), containing high glucose and vitamin concentrations and no growth factors. It was supplemented with Knockout Serum Replacement (KSR, Thermo Fisher Scientific) as surrogate for Fetal Bovine Serum (FBS), MEM Non-Essential Amino Acids Solution (MEM-NEAA, Thermo Fisher Scientific) to increase cell growth and viability, sodium pyruvate (Thermo Fisher Scientific) as carbon source besides glucose, 2-mercaptoethanol (Thermo Fisher Scientific) in order to reduce toxic ROS concentrations and penicillin-streptomycin (Thermo Fisher Scientific) to avoid bacterial contamination. After counting the cells using a Neubauer counting chamber (VWR) and Trypan Blue solution (Sigma-Aldrich), the suspension was diluted with CDMI in order to achieve a final concentration of 90,000 cells per ml. This seeding suspension was supplemented with 20 μM ROCK inhibitor to increase cell survival and 5 μM TGF-β inhibitor SB431542 (Cayman Chemical) to enhance iPSC differentiation into forebrain identity as well as 3 μM WNT antagonist I (IWR1, EMD Millipore Corporation) to induce more rostral than caudal structures.[9,81]

In order to promote formation of neurospheres, the supplemented seeding suspension was distributed to low attachment U-bottom 96-well plates (faCellitate) by adding 100 μl per well (Figure 1A), representing DIV 0 of organoid generation. 96-well plates were kept at 37°C and 5% CO_2. On DIV 3, the sides of the 96-well plates were carefully tapped in order to detach dead cells, and 100 μl of CDMI supplemented with 20 μM ROCK inhibitor, 3 μM IWR1 and 5 μM SB431542 were added per well. On DIV 6, 9, 12 and 15, 80 μl of the supernatant medium were removed from each well and replaced with 100 μl of CDMI, supplemented with 3 μM IWR1 and 5 μM SB431542 per well. The size of developing neurospheres/organoids was monitored by taking images of at least five organoids per batch every fortnight using an Eclipse Ts2 light microscope (Nikon) or a DMS1000 microscope (Leica) (Figure 1A).

From DIV 18 on, organoids were cultured in 100 mm petri dishes (Greiner Bio-One) (Figure 1A). To achieve a smooth transfer from the 96-well plates into the petri dishes, organoids were carefully taken up with a blunt 1000 μl pipette tip. The latter was filled with 5 ml CDMII (Figure 1A), consisting of DMEM/F12 (Thermo Fisher Scientific) as basal medium for supporting cell growth, GlutaMAX™ Supplement (Thermo Fisher Scientific) as a stable alternative to L-glutamine that supports cell viability, N-2 (Thermo Fisher Scientific) medium to enhance neuronal growth, Chemically Defined Lipid Concentrate (Thermo Fisher Scientific) as FBS surrogate and again penicillin-streptomycin against bacteria. After their transfer, the medium was removed again and 10 ml of fresh CDMII were added. Petri dishes were placed on an orbital shaker (Heidolph) at 70 rpm in order to guarantee sufficient oxygen and nutrient diffusion and to prevent attachment and kept at 37°C and 5% CO_2. One day after this transfer, organoids were visually examined and the speed of the orbital shaker adapted to prevent their aggregation or attachment to the bottom of the dish. CDMII was changed every second day.

On DIV 35, CDMII was replaced with freshly prepared CDMIII that in addition contained FBS (Thermo Fisher Scientific) and heparin (Sigma-Aldrich) (Figure 1A). Depending on the growth rate of the organoids (as indicated by colour changes of the medium), CDMIII was changed every two to four days. From DIV 70 on, organoids were kept in CDMIV (Figure 1A), in which B27 was supplemented by vitamin A (Thermo Fisher Scientific) to support further differentiation and growth of neuronal cells. Again, the medium was changed every 2–4 days depending on the growth rate of the organoids. Organoids were cultured for up 70–79 days until used for preparation of cortical organoid slices (Figure 1A).

The AggreWell-based protocol for generating cortical brain organoids was earlier described by Miura and colleagues.[27] iPSCs were washed and detached as explained above, and then centrifuged at 200 rcf for 4 minutes at room temperature. The resulting cell pellet was resuspended with iPS Brew supplemented with 10 μM ROCK inhibitor and consequently diluted to a concentration of 1.83 million cells/ml. 1.5 ml of the adjusted cell suspension were added per well to an AggreWell™ 800 plate (Stemcell Technologies) that was previously coated with Anti-Adherence Rinsing solution (Stemcell Technologies) for 15 minutes to acquire a total amount of 2.75 million cells per well. The AggreWell plate was centrifuged at 100 rcf for 3 minutes.

After 24 hours, the developed spheroids were transferred to 100 mm petri dishes with a cut-off 1000 μl pipette tip and kept in medium consisting of Knockout™ DMEM (Thermo Fisher Scientific), KSR, MEM-NEAA, sodium pyruvate, pencillin-streptomycin, GlutaMAX™ Supplement and MycoZap Plus-CL (Lonza). For neural induction, medium was supplemented with 2.5 μM dorsomorphin (Sigma) and 10 μM SB431542. Daily media changes were performed from DIV 2 to DIV 5.

To enhance differentiation, neurospheres were cultured in Neurobasal-A medium (Thermo Fisher Scientific) with GlutaMAX™ Supplement, pencillin-streptomycin, MycoZap Plus-CL and B-27™ Supplement (50x) minus Vitamin A (Thermo Fisher Scientific) from DIV 6 to DIV 46. Medium was changed daily between DIV 6 and DIV 15 and supplemented with 20 ng/ml EGF and FGF2 (R&D Systems). From then on, medium was changed every other day, supplemented with 20 ng/ml EGF and FGF2 (DIV 16 – 21), and then with 20 ng/ml BDNF (MACS Miltenyi), 20 ng/ml NT-3 (Peprotech), 200 μM (+)-sodium L-ascorbate, 50 μM dibutyryl cAMP (Stemcell Technologies) and 10 μM cis-4,7,10,13,16,19-docosahexaenoic acid (DHA, Millipore) (DIV 22 – 45). Long-term culture until DIV 70 was performed in the same medium with B-27™ Supplement without any further small molecules.

Immunohistochemistry of organoids

Immunofluorescence staining of organoids was performed following established protocols.[25] In brief, organoids at DIV 70 were washed three times with PBS and subsequently incubated in PBS/4% paraformaldehyde (PFA, Thermo Fisher Scientific) for one hour at room temperature. Afterwards, organoids were washed three times with PBS. Fixed organoids were stored in PBS at 4 °C until slicing. For slicing, up to five organoids were embedded into a custom-made tissue mold (cut end of a 10 ml syringe) that was filled with liquified agar (3% in PBS; Sigma-Aldrich).

Agar blocks containing organoids were cut at a vibratome (Microm HM 650 V, Thermo Fisher Scientific; amplitude 1.0 mm, frequency 60 Hz, velocity 13 mm/s) with a pre-cleaned razor blade (Wilkinson Sword) in ice-cold PBS at 100 μm thickness. Sections were gently transferred into PBS-containing well plates for intermediate storage and were finally transferred to microscope slides (SuperFrost). The agar and excessive PBS were removed from the slides using a syringe (Braun). Slices were allowed to dry till their adherence to the slides, and were stored in PBS at 4 °C until staining.

For immunofluorescence labelling, mounted organoid slices were blocked and permeabilized for one hour at room temperature with a blocking solution (10% donkey serum, 0.1% Tween 20 and 1% Triton X-100 (all Sigma-Aldrich) in PBS). Primary antibodies solved in blocking solution were applied on the slides and incubated at 4°C overnight, followed by 10 minutes' rinses in PBS for three times. Subsequently, organoid slices were exposed to secondary antibodies (diluted in blocking solution containing Hoechst dye (1: 2,500; Thermo Fisher Scientific)) for one hour at room temperature, again rinsed for 10 minutes in PBS for three times and finally mounted in ProLong Glass Antifade Mountant mounting medium (Thermo Fisher Scientific). Nail polish was used to seal the slides, which were stored at 4°C until their analysis.

Primary antibodies used here include mouse anti-β-Tubulin III (Invitrogen, T8578, 1:2000), rabbit anti-PAX6 (BioLegend, 901301, 1:200), guinea pig anti-GFAP (SynapticSystems, 173004, 1:500), rabbit anti-CTIP (Abcam, ab82701, 1:100), guinea pig anti-MAP2 (Synaptic Systems, 188004, 1:1000) rabbit, anti-Synapsin 1 (Invitrogen, A-6442, 1:500), guinea pig anti-VGLUT1 (Synaptic Systems, 135304, 1:500), rabbit anti-Homer1 (Synaptic Systems, 160003, 1:200) and mouse anti-PSD95 (Abcam, ab2723, 1:500). Secondary antibodies used here include donkey anti-guinea pig 488 (Sigma-Aldrich, SAB4600033, 1:300), donkey anti-rabbit 488 (Invitrogen, R37118, 1:300, donkey anti-mouse Cy3 (AP192C, Millipore, 1:300) and donkey anti-rabbit Cy3 (Jackson, 711-165-152, 1:300).

Specific structures of interest within organoid slices were documented using a motorized confocal laser scanning microscope C1 (Nikon) and a 20x dry objective (Plan Apo VC 20× / 0.75 air DIC N2 ∞/0.17 WD 1.0, Nikon). Images were acquired using the imaging software EZ-C1 Silver Version 3.91 (Nikon) and fluorophores were excited using three different excitations wavelengths (408, 488 and 543 nm). Z-stacks (10–30 steps) were generated from optical sections of 1.1 μm each. For visualization, extended focus projections were generated employing ImageJ software.

Electron microscopy

Organoids (DIV 107) were fixed using 3% glutaraldehyde (Serva) buffered with 0.1 M sodium cacodylate (Serva) buffer, pH 7.2. After fixation, organoids were washed with 0.1 M sodium cacodylate buffer, pH 7.2 and stained using 1% osmium tetroxide (Science services) for 50 minutes at room temperature. Samples were washed two times with 0.1 M sodium cacodylate buffer and once with 70% ethanol followed by staining with 1% uranyl acetate (Merck) / 1% phosphotungstic acid (Merck) in 70% ethanol for one hour. Samples were dehydrated and incubated with pure Spurr resin at room temperature for two hours. Spurr resin was prepared by mixing embedding medium ERL-4221D (Epoxycyclohexylmethyl-3,4-epoxycyclohexylcarboxylate, Serva), D.E.R.® 736 (Serva), Nonenylsuccinic Anhydride Pure (Serva) and Dimethylaminomethanol (Serva). Subsequently, samples were embedded in Spurr resin for polymerization at 70°C for at least 48 hours.

Ultrathin sections of 60–70 nm size were prepared using an ultra-microtome (EM UC7, Leica with a Diatome Ultra 45° knife). Electron microscopic images were acquired using a JEM-2100 plus (JOEL) equipped with an EM-24830 flash CMOS camera system (JOEL). The electron microscope was operated at 200 kV and images were acquired at the magnification of 50,000×. The images were visualized using freely available ImageJ software.

Generation of cortical brain organoid slices

The generation of cortical brain organoid slices (cBOS) was based on previous protocols described for unguided human brain ALI-COs[18] and organotypic tissue slices of the mouse brain[28,82] (Figure 1B). Notably, and in difference to Giandomenico and colleagues,[18] slices were prepared from regionalized cortical organoids established following our published protocol.[25] Apart from these differences, note especially the differences in media composition for organoid preparation and slice maintenance between the originally described ALI-CO's[18] and our protocol.[25] In addition, several washing steps with visual inspection were introduced before transferring slices onto membranes and slices were maintained at 36°C (here) instead of 37°C.[18] In more detail, 3% LMP agarose (Thermo Fisher Scientific) was diluted in HBSS (Sigma-Aldrich), heated to 90°C and slowly cooled down to 40°C. Next, single cortical organoids (DIV 70–79) were transferred into a 35 mm petri dish (Sarstedt) filled with HBSS by using a blunt 3 ml Pasteur pipette (VWR) and carefully washed by pipetting them up and down. To prepare their embedding, a custom-build mold (cut end of a 10 ml syringe) was positioned onto a piece of absorbent filter paper and LMP agarose added to its bottom. Single organoids were put onto a spatula, excessive PBS was carefully removed with filter paper and the organoid was placed into the mold. Up to five organoids were placed in one mold, which was filled with LMP agarose until all organoids were covered. Molds were stored in a glass petri dish on ice for a maximum of 10 minutes, until the agarose solidified.

For slicing, agarose blocks were carefully removed out of the mold and glued using a super glue gel (UHU) onto a mounting plate. The latter was placed in a bath filled with ice-cold HBSS. 300 μm thick slices of organoids were cut with a pre-cleaned razor blade (Wilkinson Sword) at a vibratome (Microm HM 650 V, Thermo Fisher Scientific). After cutting, slices were collected using the reverse end of a glass Pasteur pipette (Brand) and transferred to an HBBS-filled petri dish. The dish was placed onto a sterile bench, where slices were immediately transferred into a new petri dish containing pre-warmed HBSS (36°C). The latter procedure was repeated four times changing pipette and dish with every wash. Wells of a 6-well plate (Sarstedt) were filled with 750 μl of pre-warmed (36°C) CDMIV and the membrane of a cell culture insert (Millipore) positioned into each well. Up to five slices were placed onto one membrane and cultured at the air-liquid interface in a humidified atmosphere at 36°C and 5% CO_2 for additional 28–73 days. Quality control via visual inspections of each slice was performed after the slicing procedure and after the washing steps to discard slices that were obviously mechanically damaged. The medium (CDMIV) was changed daily.

Immunofluorescence staining and documentation of immunolabelled cBOS

For immunofluorescence staining (Figure 1C), individual cBOS were cut out of the culture insert and washed in PBS. Afterwards, slices were fixed in PBS/4% PFA (Sigma-Aldrich) for 20 minutes at room temperature and washed again for three times in PBS. Slices were then either stained on SuperFrost slides (VWR), for which a droplet of PBS was put onto the slide in which a single slice was placed using a spatula. Alternatively, slices were stained in well plates. In both cases, several rings of Fixogum (Marabu) were applied around the slices to protect the tissue from damage during the embedding procedure. Excessive PBS was removed using a syringe and slices were shortly dried until they adhered to the coating.

For permeabilization and blocking, slices were incubated for one hour at room temperature with a blocking solution consisting of PBS, 10% goat serum (Thermo Fisher Scientific) and 1% Triton X-100 (AppliChem). Next, the blocking solution was aspirated and the desired primary antibody concentration diluted in blocking solution was added. Primary antibodies were incubated overnight at 4°C in a humidified chamber, washed three times for 10 minutes in PBS and then incubated with the secondary antibodies in blocking solution. From there on, slices were kept in darkness. Slices were again washed three times for 10 minutes in PBS and DAPI (1.2 μM in PBS, Thermo Fisher Scientific) was applied for 20 minutes. Three washing steps in PBS followed. Last, slices were mounted in the embedding medium Mowiol (contains DABCO to prevent bleaching; Millipore) and carefully covered by a cover glass. Slices were allowed to rest for at least 30 minutes before sealing with nail polish. Alternatively, same blocking as well as antibody solutions were directly applied on single slices in a 24 well-plate. Slices were then

transferred via a spatula on SuperFrost slides, excessive PBS was removed, slices were embedded in Mowiol and covered by cover glasses. Each staining was performed on at least 3 different slices. Negative controls were done in parallel to each staining.

Unless otherwise stated, the same primary antibodies were used as for cortical organoids. Additionally, the following primary antibodies were used: rabbit anti-S100ß (Abcam, ab52642, 1:600), rabbit anti-GFAP (Dako, ZO334, 1:1000) and mouse anti-PSD95 (Millipore, MABN68, 1:500). The following secondary antibodies were used: goat anti-guinea pig 488 (Invitrogen, A-11076, 1:300), goat anti-guinea pig 594 (Invitrogen, A-11076, 1:300), goat anti-rabbit 488 (Invitrogen, A-11008, 1:300), goat anti-rabbit 594 (Invitrogen, A-11012, 1:300), goat anti-mouse 488 (Invitrogen, A-11001, 1:300) and goat anti-mouse 594 (Invitrogen, A-11005, 1:300).

A stereo microscope SMZ25 (Nikon) equipped with a 2x dry objective (SHR Plan Apo 2x, WD 20, Nikon) and the software NIS-Elements BR 4.50.00 (Nikon) or a motorized Eclipse 90i upright wide field microscope (Nikon) equipped with a 4x dry objective (Plan Fluor 4x /0.13 air ∞/- WD 17.1, Nikon) and a 10x dry objective (Plan Fluor 10x / 0.30 air DIC L/N1 ∞/0.17 WD 16, Nikon) were used for documentation of overview stitches. For image acquisition, the imaging software NIS-Elements Advanced Research 3.2 (Nikon) combined with a DS-Q1Mc camera (Nikon) and the DAPI filter set (340–380 nm, dichroic mirror: 400 nm, barrier filter: 435–485 nm) were used. Cellular structures were documented by a motorized confocal laser scanning microscope (Nikon Eclipse C1 mounted on an E600FN, Nikon) equipped with a 20x dry objective (Plan Apo VC 20x / 0.75 air DIC N2 ∞/0.17 WD 1.0, Nikon), a 60x oil objective (Plan Apo VC 60x / 1.40 oil DIC N2 ∞/0.17 WD 0.13, Nikon) and a 100x oil objective (Plan Apo VC 100x/ 1.40 oil DIC NC ∞/0.17 WD 0.13, Nikon). The imaging software EZ-C1 3.91 Silver Version (Nikon) was employed for image acquisition. The following excitation lasers were used: 408 laser (Coherent), Argon laser (488 nm, Melles Griot) and Helium-Neon laser (543 nm, Melles Griot); filter sets for emission light were: 450/25, 515/30 and 605/75. Confocal z-stacks (41–122 steps) were generated with optical sections of 0.6 μm each. Individual images represent an average of three consecutive frames. Volume-view images of MAP2-positive structures were analyzed by NIS-Elements Advanced Research 5.0 (Nikon) using an Alpha Blending setting.

Propidium iodide nucleic acid stain

PFA-fixed cBOS were incubated in Triton/PBS for 15 minutes and equilibrated in 2X SSC (0.3 M NaCl, 0.03 M sodium citrate, pH 7.0) two times. Samples were incubated in 100 μg/mL DNase-free RNase in 2X SSC for 20 minutes at room temperature and rinsed for three times in 2X SSC. Afterwards, slices were incubated with Propidium Iodide (500 nM; 1:3000) for five minutes, followed by three washing steps in 2X SSC. Finally, slices were embedded in Mowiol and covered by a cover glass. A stereo microscope SMZ25 (Nikon) equipped with a 2x dry objective (SHR Plan Apo 2x, WD 20, Nikon) and the software NIS-Elements BR 4.50.00 (Nikon) were used for the documentation of overview images.

Whole-cell patch-clamp recordings

Somatic whole-cell patch-clamp recordings (Figure 1C) were performed at an upright microscope (BX51WI, Olympus), equipped with a water immersion objective (NIR Apo 60x/ 1.0 water DIC N2 ∞/0 WD 2.8, Nikon), using an EPC10 amplifier and "PatchMaster"-software (HEKA Elektronik). cBOS were transferred into a custom build microscope perfusion chamber and constantly perfused with standard ACSF at a rate of about 2.5 ml/min at room temperature (22 ± 1°C). ACSF contained (in mM): 130 NaCl, 2.5 KCl, 2 $CaCl_2$, 1 $MgCl_2$, 1.25 NaH_2PO_4, 26 $NaHCO_3$, and 10 glucose; pH 7.4, bubbled with carbogen (95% O_2 and 5% CO_2); osmolarity ~310 mOsm/l.

Measurements were performed using 3–6 MΩ patch pipettes pulled from borosilicate glass capillaries (Hilgenberg) using a vertical puller (PP-830, Narishige). Pipettes were filled with an intracellular solution containing (in mM): 114 K-$MeSO_3$, 32 KCl, 10 HEPES, 10 NaCl, 4 Mg-ATP and 0.4 Na_3-GTP; pH adjusted to 7.3 with KOH. Liquid junction potential was not corrected. Cells were held in the current or voltage clamp mode. Data were sampled at 1 kHz and processed and analyzed employing Origin Pro 2021 Software (OriginLab Corporation) and Excel (Microsoft Office Professional Plus 2019).

For visualization of the morphology of the recorded cells, 200 μM Alexa 488 (Thermo Fisher Scientific) was added to the intracellular saline. Cells were documented using a custom-build multi-photon microscope based on a Fluoview300 system (Olympus) using a water immersion objective (NIR Apo 60x/ 1.0 water DIC N2 ∞/0 WD 2.8, Nikon). Excitation wavelength was 840 nm; fluorescence emission was collected below 700 nm. Cellular morphology was documented by recording z-stacks with 1 μm increments in-between focal planes using the software FluoView5.0 (Olympus).

Imaging of intracellular calcium

For imaging of spontaneous calcium signals (illustrated in Figures 6A–6C), a wide field system composed of an upright microscope (Eclipse FN-1, Nikon), a 40x water immersion objective (Fluor 40x/ 0.8 water DIC M/N2 ∞/0 WD 2.0, Nikon), an Orca FLASH 4.0LT camera (Hamamatsu Photonics) and a Polychrome V monochromator (Thermo Fisher Scientific) were used. Results illustrated in Figures 6D–6G were obtained at a wide field system composed of an upright microscope (Eclipse FN-1, Nikon) equipped with a 40x water immersion objective (LUMPlanFL 40x/ 0.8 water ∞/0 WD 3.3, Olympus), an Orca FLASH 4.0 camera (Hamamatsu Photonics) and a Polychrome V monochromator (Thermo Fisher Scientific).

Single cBOS were placed into a recording chamber, fixed by a grid and continuously perfused (~2.5 ml/min) with standard ACSF (see above) for measurements performed at room temperature (22 ± 1°C). For measurements at 37 ± 1°C, a modified ACSF was used, containing (in mM): 138 NaCl, 2.5 KCl, 1.25 NaH_2PO_4, 18 $NaHCO_3$, 2 $CaCl_2$, 1 $MgCl_2$, and 10 glucose; pH 7.4, bubbled with carbogen (95% O_2 and 5% CO_2); osmolarity ~310 mOsm/l. Slices were allowed to equilibrate for about 15 minutes, after which the calcium indicator Oregon Green 488 BAPTA-1-acetoxymethyl ester (OGB-1-AM, 200 μM; Thermo Fisher Scientific; Stock concentration: 1 mM solubilized in 20%Pluronic/DMSO) was bolus-injected into the extracellular space using a fine glass pipette. Slices were incubated for another 30 minutes to allow for

de-esterification before the start of the measurements. OGB-1 was exited at 488 nm and fluorescence emission was collected >500 or >505 nm at a frequency of 1 Hz or 5 Hz from regions of interest (ROIs) representing individual cell bodies. Active cells displayed at least one calcium signal (defined by a peak amplitude > 5x S.D. of baseline) during a recording period of 5 minutes (control and with TTX added).

Experiments were controlled and analyzed by NIS-Elements Advanced Research 5.0 (Nikon). Signals from individual ROIs were background corrected, exported to Excel (Microsoft Office Professional Plus 2016) and normalized to baseline. Afterwards, traces were bleaching corrected and further analyzed employing OriginPro 2020 (OriginLab Corporation).

Receptor agonists and antagonists were added to the ACSF and bath-applied via the perfusion system. Antagonists were added 15 minutes before the start and during the entire course of imaging experiments. Chemicals were purchased from Merck/Sigma-Aldrich or AppliChem if not stated otherwise. TTX and DL-2-Amino-5-Phosphonovaleric (DL-APV) acid were obtained from Biozol/HelloBio; 2,3-Dioxo-6-nitro-1,2,3,4-tetrahydrobenzo[f]quinoxaline-7-sulfonamide disodium salt (NBQX) was obtained from Biotrend. Chemical ischemia was induced by perfusing cBOS with glucose-free modified ACSF containing 5 mM of the cytochrome c oxidase inhibitor sodium azide (Honeywell) and 2 mM of the glucose analogue 2-Deoxy-D-glucose (Apollo Scientific) for two minutes.

Imaging of intracellular ATP

Imaging of intracellular ATP was performed using the FRET-based sensor ATeam1.03^{YEMK} ("ATeam"; Figure 1C). Expression of ATeam under the neuron-specific human synapsin 1 promotor fragment hSyn1 was induced by a single-stranded adeno-associated-vector (AAV; ssAAV-2/2-hSyn1-ATeam1.03^{YEMK}-WPRE-hGHp(A), ETH Zürich). cBOS at DIV 94–101 in culture were transduced by diluting the AAV 1:1 (virus titer: 3.1 x 10^{12} genome/ml) in dPBS and applying 1 µl of the solution on top of each slice.[82] After transduction, slices were cultured for additional 10–25 days in a humidified atmosphere at 36°C and 5% CO_2 in the presence of CDMIV.

Transduced slices were transferred to a wide field imaging system composed of an upright microscope (Eclipse FN1, Nikon) equipped with a 40x water immersion objective (Fluor 40x / 0.80 water DIC M ∞/0 WD 0.8, Nikon), an Orca 4 LT Plus CMOS camera (Hamamatsu Photonics) and a Polychrome V monochromator (Thermo Fisher Scientific) (Figure 1 C). cBOS were placed in a recording chamber, fixed with a grid and continuously perfused (~2.5 ml/min) with modified ACSF (see above) at 37 ± 1°C.

ATeam was excited at 434 nm and images were acquired at 0.5 Hz. The fluorescence emission was split at 500 nm by an image splitter (WVIEW GEMINI optic system, Hamamatsu Photonics) and the two channels subsequently band-pass filtered at 483/32 (eCFP, donor) and 542/27 (mVenus, acceptor). For analysis, NIS-Elements Advanced Research 4.5 (Nikon) was used. Signals from individual ROIs representing cell somata were background-corrected, the ratio Venus/eCFP was calculated and data exported to Excel (Microsoft Office LTSC Professional Plus 2021) to normalize traces to their initial baseline. For further analysis, OriginPro 2021 (OriginLab Corporation) was employed. Transient inhibition of cellular ATP production ("chemical ischemia") was induced by perfusing cBOS with metabolic inhibitors for 2 minutes as described above.

Image processing and preparation of figures

Processing of images from immunohistochemistry was performed using the software ImageJ.[83] Averaged single-plane images or z-stacks were converted into 8-bit tif-files. Maximum-intensity projections (MIPs) were generated out of z-Stacks. Single channels were merged and merges saved as RGB Color tif-files. For illustration purposes, the brightness and contrast of single-plane images as well as maximum intensity projections (MIPs) were adjusted using ImageJ and/or Photoshop CS6 (Adobe Inc.). Stitches were cropped and the scale bars were calculated using ImageJ. EM images were additionally processed using Photoshop CS6 (Adobe Inc.). Figures were composed using the vector graphic editor Affinity Designer 1.9 (Serif Europe).

QUANTIFICATION AND STATISTICAL ANALYSIS

Results from statistical analysis are reported in the results section and figures. Data are illustrated in box plots representing the mean (red squares), median (black lines), 25/75 percentiles (boxes) and 1x SD (whiskers). Single data points are shown as grey diamonds.

For statistical evaluation, data was analyzed by a Kolmogorov-Smirnov normality test (sample sizes $n \geq 50$).[84] Non parametric data were tested via Mann-Whitney U test.[85] "n" represents the number of analyzed cells and "N" the number of analyzed slices. Alpha values are represented as follows: ***: $p < 0.001$; **: $0.001 \leq p < 0.01$, *: $0.01 \leq p < 0.05$ and not significant: $p \geq 0.05$. Sets of experiments are based on one to three different batches of cortical organoids.